Accepted Manuscript

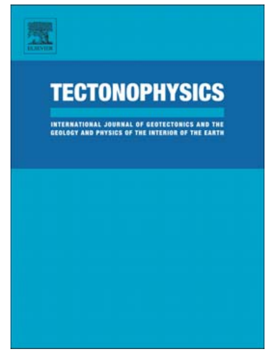

Refertilization process in the Patagonian subcontinental lithospheric mantle of Estancia Sol de Mayo (Argentina)

Massimiliano Melchiorre, Massimo Coltorti, Michel Gregoire, Mathieu Benoit

PII: S0040-1951(15)00132-8
DOI: doi: 10.1016/j.tecto.2015.02.015
Reference: TECTO 126554

To appear in: *Tectonophysics*

Received date: 28 May 2014
Revised date: 28 January 2015
Accepted date: 16 February 2015

Please cite this article as: Melchiorre, Massimiliano, Coltorti, Massimo, Gregoire, Michel, Benoit, Mathieu, Refertilization process in the Patagonian subcontinental lithospheric mantle of Estancia Sol de Mayo (Argentina), *Tectonophysics* (2015), doi: 10.1016/j.tecto.2015.02.015

Refertilization process in the Patagonian subcontinental lithospheric mantle of Estancia Sol de Mayo (Argentina)

Massimiliano Melchiorre[1,2,*], Massimo Coltorti[1], Michel Gregoire[3], Mathieu Benoit[3]

(1) Department of Physics and Earth Science, Ferrara University, via Saragat 1, 44123 Ferrara, Italy.

(2) Institute of Earth Sciences Jaume Almera – CSIC, C. Luís Solé i Sabarís s/n, 08034 Barcelona, Spain.

(3) Géosciences Environment Toulouse, CNRS-IRD-Toulouse University, Midi-Pyrénées Observatory, 14 Av. E. Belin, 31400 Toulouse, France.

* Corresponding author: Massimiliano Melchiorre, , Institute of Earth Science Jaume Almera – CSIC, Barcelona, Spain. *E-mail address:* mmelchiorre@ictja.csic.es

Abstract

Anhydrous mantle xenoliths equilibrated at 1003-1040°C from Estancia Sol de Mayo (ESM, Central Patagonia, Argentina) and entrained in post-plateau alkaline lavas belonging to Meseta Lago Buenos Aires have been investigated aiming at reconstructing the depletion and enrichment processes that affected this portion of the Patagonia lithospheric mantle. Xenoliths are characterized by a coarse-grained protogranular texture and are devoid of evident modal metasomatism. They show two texturally different clinopyroxenes: protogranular (cpx1) and texturally related to spinel (cpx2). Three different types of orthopyroxenes are also recognized: large protogranular crystals with exsolution lamellae (opx1); small clean and undeformed grains without exsolution lamellae (opx2) and small grains arranged in vein (opx3). Major element composition of clinopyroxenes and orthopyroxenes highlights two different trends characterized by i) high Al_2O_3 content at almost constant mg# and ii) a slight increase in Al_2O_3content with decreasing mg. Clinopyroxenes are enriched in LREE and are characterized by prominent to slightly negative Nb, Zr and Ti anomalies. No geochemical differences are observed between cpx1 and cpx2, whilst a discrimination can be observed between opx1 and opx2 (LREE-depleted; prominent to slightly negative Ti and Zr anomalies) and opx3 (prominent positive Zr anomaly). Partial melting modelling using both major and trace elements indicates a melting degree between ~ 5% and ~ 13% (up to ~ 23% according to major element modelling) for lherzolites and between ~ 20% and ~ 30% for harzburgites (down to ~ 5% according to trace element modelling). La/Yb and Al_2O_3, as well as Sr and Al_2O_3 negative correlation in clinopyroxenes point to a refertilization event affecting this lithospheric mantle. The agent was most probably a transitional alkaline/subalkaline melt, as indicated by the presence of orthopyroxene in vein and the similar geochemical features of ESM clinopyroxenes and those from Northern Patagonia pyroxenites which are derived from transitional alkaline/subalkaline lavas.

Key words: Patagonia, mantle xenoliths, refertilization, T-P-fO_2 conditions

1. Introduction

Xenoliths of sub-arc mantle entrained in arc magmas are rarer than those from intra-plate settings, i.e. from oceanic hotspots and continental rift zones (*Nixon, 1987*). Thus a paucity of xenolith-based, direct petrological information of the mantle wedge exists and a systematic investigation of the rare occurrences of these xenoliths needs to be carried out. Within subduction settings two groups of xenoliths can be distinguished taking into account the composition of the host magma, i.e. alkaline and calc-alkaline s.l. lavas. The type locality of xenoliths entrained in alkaline basalts in back arc zones is Patagonian, but several occurrences have been found also in the Mediterranean area [Tallante, *Bianchini et al., 2011*; Pannonian Basin, including Styrian Basin (Kapfenstein, *Kurat et al., 1980*; *Coltorti et al., 2007*, Bakoni–Balaton Highlands, *Bali et al., 2008*; *Hidas et al., 2010*; *Berkesi et al., 2012*)]. Xenoliths entrained in calc-alkaline basalts s.l. are those belonging to the Japan arc (*Takahashi 1978*; *Aoki 1987*; *Arai et al . 1998*), the Kamchatka arc (*Koloskov and Khotin, 1978*; *Kepezhinskas et al., 1995; Arai et* *al., 2003; Widom et al., 2003; Saha et al., 2005; Weyer & Ionov, 2007; Ionov and Seitz, 2008*), and the Tabar–Lihir–Tanga–Feni arc (Papua New Guinea, *McInnes et al. 2001*; *Franz et al., 2002*).

Widespread metasomatic evidences have been documented in the Patagonian sub continental lithospheric mantle by various authors. In many cases mantle xenoliths entrained in the back-arc Patagonian lavas from various localities (between 40°S and 52°S) record regional, pervasive re-crystallisation leaving only a few relics of the preceding mantle texture. Cryptic [trace element enrichments of clinopyroxenes (cpx)] and modal (crystallization of hydrous phases such as amphibole ± phlogopite) metasomatism occur in most of the studied suites. The point is to define the nature and to understand the origin of the metasomatic melts that affect the mantle and that generate the observed textural and geochemical features. Some authors attribute the metasomatic agent/s to silicate melts similar to the host lavas as for Pali Aike (*Kempton et al., 1999; Stern et al. 1999*). *Gorring and Kay (2000)* provide information about a possible involvement of a carbonatite melt at Gobernador Gregores, while a plume-related melt has been inferred by *Bjerg et al (2005)* for the Patagonian mantle. Slab derived metasomatism has been proposed for one of the westernmost localities (i.e. the closest to the trench) represented by Cerro del Fraile (*Kilian et al., 1998*; *Kilian and Stern, 2002*; *Faccini et al., 2013*), as well as for Cerro de los Chenques (*Rivalenti et al., 2007*), Gobernador Gregores and Pali Aike (*Stern et al., 1989; Laurora et al., 2001*).

In this study we present new major and trace element compositions of a suite of mantle xenoliths sampled at Estancia Sol de Mayo (ESM), belonging to Meseta Lago Buenos Aires (MLBA, **Fig. 1B**), which is one of the five back-arc Mesetas situated between 46° and 49°S. Our aim is to identify the refertilization processes that could have affected this Central Patagonia locality and to constrain the origin of the melts that have percolated into and interacted with the mantle.

2. Geological setting

In Patagonia the Andean volcanic arc is distinguished into a Southern Volcanic Zone (SVZ; *Thorpe et al., 1982*) and an Austral Volcanic Zone (AVZ; *Stern and Kilian, 1996*) separated by a volcanic gap occurring between 46.30° and 49.00°S latitude. The geological history during the Cenozoic for both SVZ and AVZ is related to the subduction of the Nazca (convergence rate of 10 cm*yr^{-1}) and Antarctic (convergence rate of 2 cm*yr^{-1}) plates beneath the South American plate. The two plates are separated by the Chile ridge, and the present day position of the triple point between the Nazca, South American and Antarctic plates (Chile Triple Junction, CTJ) occur at 46.30°S. (*Cande and Leslie, 1986*; *Forsythe et al., 1986*).

A peculiar feature of Patagonia is the presence of several continental mafic volcanic plateaus ranging in age from late Paleocene to Recent times (*Ramos and Kay, 1992*) (**Fig. 1A**). The sequence pre-plateaus – main plateaus – post-plateaus is usually recognized, with the second stage being the most voluminous. The Somoncura igneous province, the largest post-Eocene mafic volcanic field of Northern Patagonia, occurs between ~ 40°S and 46°S. It consists of a series of Oligocene to early Miocene volcanic fields that cover more than 55,000 km^2 in the Meseta de Somuncura and surrounding region (Meseta de Cari Laufquen and Meseta de Canquel), overlying a late Precambrian to Paleozoic magmatic and metamorphic basement itself covered by the extensive Jurassic silicic volcanic rocks of the Chon Aike province (*Kay et al., 1989*; *Pankhurst and Rapela, 1995; Kay et al., 2007*), as well as Cretaceous to Tertiary volcanic and sedimentary rocks (*Rapela and Kay, 1988*; *Rapela et al., 1988*; *Ardolino et al., 1999*). Oligocene intraplate alkaline basalts and hawaiites are typical of the pre-plateau stage, followed by a voluminous ~27±2 Ma hyperstene-normative basalt and basaltic andesite plateau sequence and by intermediate to low volume post-plateau alkali olivine basalts and hawaiites (~23-17Ma) (*Kay et al., 2007).*

In Central Patagonia (between 46°S and 49°S) the middle Miocene to Recent northward migration of the CTJ from approximately 50°S (*Cande and Leslie, 1986*; *Forsythe et al., 1986*) to 46.30°S has generated unique geodynamic, structural and magmatic features (*Gorring et al., 1997*), namely the modern volcanic arc gap between the SVZ and the AVZ, the eruption of arc adakitic magmas (*Kay et al., 1993*) and finally the extensive late Miocene to Pleistocene magmatism that originated the Triple Junction Province (TJP). It can be subdivided into a voluminous, late Miocene to early Pliocene main plateau sequence, and a less voluminous, latest Miocene to Plio-Pleistocene post-plateau sequence (*Gorring et al., 1997*). The main plateau sequence forms the smaller mesetas to the northeast (called “northeastern region”) and the large and elevated plateaus of the de la Muerte (MM), Belgrano (MB), Central (MC) and Lago Buenos Aires (MLBA) Mesetas (**Fig. 1B**). The post-plateau sequence comprises small scoria cones, as well as lava flows and pyroclastic deposits capping the main plateau sequence. OIB-like tholeiitic main plateau (~12-5 Ma) and alkaline post-plateau lavas (~7-2 Ma) are related to the slab window tectonic evolution (*Ramos and Kay, 1992; Kay et al., 1993; Gorring et al., 1997*).

Finally between 49°S and 52°S (i.e. Southern Patagonia) there is the occurrence of the southernmost and youngest (~3.8 Ma to Recent, *D'Orazio et al., 2000*) Cenozoic back-arc Patagonian lavas, represented by the Pali Aike Volcanic Field (PAVF), being characterized by alkaline and olivine basalts and basanites. It covers an area of about 4,500 km^2 north of the Magallanes fault system and is situated 200 km east of the Andean Cordillera. More than 80% of the totality of the volcanic products consists of an extensive succession of plateau-like basaltic lava flows, while the remaining 20% consists of more than 450 monogenetic structures represented by maars, tuff-rings, scoria and spatter cones, and associated lava flows (*D'Orazio et al., 2000*). *D'Orazio et al. (2000)* observed two main elongation trends of the cones, one with an ENE direction and another with a NW direction, the first being linked to the still active Magallanes Strait Rift System described by *Diraison et al. (1997)* while the second is probably connected with the Mesozoic Patagonian Austral Rift (*Corbella et al., 1996*).

3. Analytical methods

This study is based on the major and trace element characterization of the mineral phases of Patagonian mantle xenoliths carried out with an Electron Microprobe (EMP) and a Laser Ablation Inductively Coupled Plasma Mass Spectrometer (LA-ICP-MS). Major and trace element compositions of the entraining lavas were performed with X-Ray Fluorescence (XRF). All the analysis were performed at the UMR 5563 (LMTG, Observatoire Midi-Pyrenees) of the University Paul Sabatier (Toulouse III), except the bulk rock composition of the lava, performed at the University of Ferrara.

Major element compositions of minerals were determined with the CAMECA SX50 electron microprobe and a standard program: beam current of 20 nA and an acceleration voltage of 15 kV, 10 – 30 s of peak counting, 10 s of background counting, and natural and synthetic minerals as standards.

Nominal concentrations were subsequently corrected using the PAP data reduction method (*Pouchou and Pichoir 1984*). The theoretical lower limits of detection are about 100 ppm (0.01%).

Concentrations of REE and trace elements in cpx and orthopyroxene (opx) were determined in situ using the Agilent 7500 ICP – MS instrument coupled either with CETAC laser ablation module that uses either a 266 nm frequency-quadrupled Nd-YAG laser or a commercial femtosecond Ti : Sa laser system (Amplitude Technologies Pulsar 10) based on the Chirped-pulse amplification (CPA) technique. Pulses were amplified in this set-up by a regenerative and a multipass amplifier up to 12 mJ. This system provides laser pulses at 800 nm with variable pulse energy and pulse duration as short as 50 fs. Its contrast on 10 ps is on the order of 10^{-7}. Its repetition rate can be varied between 1 Hz and 10 Hz. The shot-to-shot stability (RMS) is 2 %. The linearly polarized laser beam is injected in a BX51 microscope (Olympus). The beam is reflected by a 45° dielectric mirror and focused down to the sample placed in an ablation cell mounted on an XY stage, using a 0.9 Cassegrain objective. The NIST 610 and NIST 612 glass standards were used to calibrate relative element sensitivities of cpx and opx, respectively (provided as supplementary data). Precision and accuracy (<5% and <20% respectively) were assessed from repeated analyses of NIST 612 and NIST 610 as unknowns. Each analysis was normalized using CaO and SiO_2 values, first determined by electron microprobe, for cpx and opx respectively. A beam diameter of 50 – 100 μm and a scanning rate of 20 μm/s were used. The theoretical limits of detection range from 10 – 20 ppb for REE, Ba, Th, U, Zr to 2 ppm for Ti..

Whole-rock major elements and some trace elements (Zn, Cu, Sc, Ga, Ni, Co, Cr, V, Rb, Ba, Th, Nb, Sr, Zr, and Y) were obtained by X-ray fluorescence (XRF) on pressed-powder pellets, using an ARL Advant-XP automated X-ray spectrometer. Calibration was performed using international reference samples (some of which were also run as unknowns in order to determine accuracy and detection limits), and the matrix correction method proposed by *Lachance and Traill (1966)* was applied. Mean accuracies were generally better than 2% for major oxides, and better than 5% for trace element determinations, while the detection limits for trace elements were: Zn, Ba, Cu, Sc = 5 ppm; Ni, Co, Cr, V, Rb, Y, Th, Nb = 1 ppm; and Sr, Zr, Ga = 2 ppm. Volatile contents were determined to be lost on ignition at 1000 °C.

4. Chemical composition of the host lavas

Six alkaline post-plateau host rocks have been analysed in this work. The samples do not represent an extensive ad hoc sampling of MLBA. Previous works on the Plio-Pleistocene post-plateau volcanism in this area (*Gorring et al., 2003*) link its origin to the opening of an astenospheric window during the subduction of the Chile Ridge beneath the Andean margin ~6 Ma ago.

The lavas analysed are quite fresh, characterized by a porphyritic texture with 2 to 5% phenocrysts. They are overwhelmingly dominated by euhedral olivine (ol), sometimes occurring in glomerophyric assemblages (in some cases surrounded by a marked rim of reaction) that, since they carry mantle xenoliths, should be of mantle origin. The groundmass is microcrystalline indicating a rapid magma cooling, with abundant acicular plagioclase, associated with cpx, ol and Fe-Ti oxides.

The geochemical composition of MLBA lavas analyzed in this study is given in **Table 1**. MLBA post-plateau lavas are sodic alkaline (~50 wt.% SiO_2; ~8 wt.% Na_2O+K_2O, with Na_2O/ K_2O >2), plotting in the basaltic trachy-andesite field on a Total Alkali–Silica classification diagram (**Fig. 2**). They have low MgO content (~4 wt. %) as well as Ni and Cr, the first being ~45 ppm and the second varying from 164 to 210 ppm.

Chondrite-normalized trace element concentrations of the samples are shown in **Fig. 3**. The patterns of the lavas in this work resemble those of the OIB, as well as those of the main and post-plateau from the TJ province, the latter having slightly higher incompatible trace element concentrations with respect to those of the main plateau. The OIB signature of the samples is also highlighted by the low Ba/Nb ratios that are less than 10 (typical of the composition within plate lavas).

5. Petrography of the samples

Fifteen xenoliths occurring in the post-plateau lavas of the MLBA have been studied. Most of them are very small in size (a few centimeters across) and are rounded in shape. Their modal composition has been calculated by counting over 1,000 points per thin section.

The xenoliths are mainly represented by anhydrous spinel-bearing harzburgites (7) and dunites (5), with minor lherzolites (2) and one wehrlite (**Fig. 4**). They are characterized by a coarse grained protogranular texture (*Mercier and Nicolas, 1975*) and they are devoid of metasomatic features, such as spongy rims, reaction rims around spinel (sp) and/or opx, glassy patches, as well as any hydrous minerals.

Common textural features are the presence of two kinds of cpx and sp, as well as three types of opx. The former generally occur as protogranular in the peridotitic matrix (cpx1, **Fig. 5A**) or growing around the sp (cpx2, **Fig. 5B**); in this case the sp is identified as "sp_{cpx}" (**Fig. 5B**), whereas when separated from the cpx it is called "sp". Opx is present as i) large protogranular crystals with exsolution lamellae of cpx (opx1, **Fig. 5A**), ii) small clean and undeformed grains without exsolution lamellae (opx2, **Fig. 5B**) and iii) as smaller grains arranged in vein (opx3, **Fig. 5C**).

6. Geochemistry of the mineral phases

6.1. Major elements

6.1.1. Olivine

Ol of lherzolites have a Fo content ranging from 90.5 to 91.3 (**Table 2**). Ol in the two lherzolite samples are characterized by a wide range of SiO_2 content, with MGP2b2 (39.5-42.1 wt. %) showing a higher variation than MGP2b (40.2-41.4 wt. %), and by a similar range of NiO (0.27-0.50 wt. %). Ol in harzburgites have Fo varying from 84.2 up to 92.1. Apart from sample MGP4b, which presents a Fo content (91.7-92.1) higher than those of lherzolitic ol and a narrow range of variation of SiO_2 (40.9-41.7 wt. %) and NiO (0.33-0.45 wt. %), the remaining harzburgites have similar or lower Fo content (89.2-90.8). Ol of harzburgites MGP1b and MGP1g have particularly low Fo (84.2-88.6) as well as SiO_2 and NiO contents, the former varying from 39.2 to 40.4 wt. % and the latter from 0.17 to 0.46 wt. % respectively. Ol of dunites (MGP1h and MGP2a) are characterized by Fo (89.4-91.4) contents akin to those of lherzolites with sample MGP1h (90.1-91.4) showing a range slightly higher than the one of MGP2a (89.4-90.1). Also the SiO_2 and NiO content variations are similar to those of lherzolites, varying from 39.6 to 41.2 wt. % and from 0.21 to 0.46 wt. %, respectively. Finally, ol of the wehrlite shows the lowest Fo values, ranging from 81.3 to 82.1. They also show low SiO_2 and NiO values, ranging, respectively, from 38.9 to 39.7 wt. % and 0.14 to 0.20 wt. %.

6.1.2. Clinopyroxene

Cpx are classified according to their textural features i.e. those occurring as protogranular (cpx1) and those linked to sp (cpx2) (**Fig. 5A** and **B**).

Cpx1 and cpx2 from lherzolites have similar mg#, the former ranging from 91.0 to 92.0 and the latter between 90.6 and 91.9. Cpx2 shows slightly higher Al_2O_3 and Cr_2O_3 (**Table 3 and Fig. 6A**) contents (4.01-4.31 wt. % and 1.19-1.45 wt. %, respectively) with respect to cpx1 (3.21-4.12 wt. %, with one reaching 4.52 wt. %, and 0.56-1.02 wt. %, respectively). Both types of cpx have similar CaO (20.9-21.6 wt. %), Na_2O (0.76-1.02 wt. %) and TiO_2 (0.12-0.39 wt. % with a couple of cpx1 having 0.05 and 0.08 wt. %) contents, whereas SiO_2 varies widely, with cpx2 marked by lower values (50.0-53.1 wt. % for cpx2 and 51.1-53.7 wt. % for cpx1).

The mg# of cpx1 from harzburgites varies from 89.9 up to 92.9; they are also characterized by higher SiO_2 (51.8-54.1 wt. %) contents than those of the lherzolites, lower Al_2O_3 (1.75-3.56 wt. %) as well as TiO_2 (0.05-0.2 wt. %) contents, but similar Cr_2O_3 (0.57-1.45 wt. %), Na_2O (0.71-1.0 wt. %), and CaO (20.8-21.7 wt. %) contents. All cpx2 (except those belonging to harzburgite MGP1b [mg# 87.9-88.9]) show a range of mg# (91.5-92.3), Al_2O_3 (3.46-4.45 wt. %), Cr_2O_3 (1.26-1.59 wt. %), CaO (21.0-21.3), and TiO_2 (0.12-0.31 wt. %) akin to those of cpx2 from lherzolite, showing a narrower range of SiO_2 (52.3-53.1 wt. %) and a higher content of Na_2O (0.95-1.18 wt. %). Cpx2 from harzburgite MGP1b do not show any compositional differences with the cpx1 from the same sample.

Cpx1 from dunites have a very narrow mg# range, from 89.5 to 91.5 similar to that in harzburgite MGP3b. They also display the same Al_2O_3 (1.75-3.12 wt. %) but with a slightly lower Cr_2O_3 (from 0.73 to 1.20 wt. %) content. At comparable mg# with harzburgites, they are characterized by higher TiO_2 (0.07-0.30 wt. %) and Na_2O (0.74-1.13 wt. %) contents (but similar to those of lherzolites) and lower SiO_2 (52.1-53.4 wt. %) and CaO (20.5-21.8 wt. %) contents. With respect to cpx1, cpx2 have mg# (89.6-90.9) similar to that of the cpx1, but have higher Al_2O_3 (2.65-4.03 wt. %) and Na_2O (1.00-1.27 wt. %), slightly higher Cr_2O_3 (0.91-1.36) and TiO_2 (0.24-0.51 wt. %) and slightly lower SiO_2 and CaO contents (varying from 51.6 to 52.8 and from 19.9 to 21.1, respectively). All these features collocate the cpx2 of dunites in the same field as those previously described for lherzolites and harzburgites (with the exception of cpx2 from harzburgite MGP1b).

Cpx of the wehrlite show the lowest mg# ranging from 81.5 to 84.6. They are characterized by the highest Al_2O_3 and TiO_2 contents (5.13 - 7.3 wt. % and 0.65 - 1.17 wt. %, respectively) and the lowest Cr_2O_3 (0.37-0.86 wt. %), CaO (15.75-21.4 wt. %), Na_2O (0.63-1.00 wt. %) and SiO_2 (49.4-51.6 wt. %) contents.

6.1.3. Orthopyroxene

Opx have been divided in three groups on the basis of their petrographic and textural features (**Fig. 5A**, **B** and **C**). No differences between opx1 and opx2 have been found in terms of major element composition, whereas opx arranged in vein (opx3, dunite MGP2a) is always quite well discriminated chemically, too.

Opx from lherzolites have mg# ranging from 90.1 to 91.5 with an Al_2O_3 content ranging from 2.62 to 2.97 wt. % (**Table 4**, **Fig. 6B**). They also show high and quite variable Cr_2O_3 (0.48-0.70 wt. %), SiO_2 (55.3-56.4 wt. %) and CaO (0.84-0.99 wt. %) contents. Opx of harzburgites are characterized by a wider mg# range varying from 84.2 to 93.0. Two samples (harzburgites MGP3b and MGP1c) have mg# akin to those of lherzolites (90.1-91.6), with lower Al_2O_3 (1.37-2.14 wt. %), slightly lower Cr_2O_3 (0.26 to 0.63 wt. %), similar CaO [0.82 and 0.97 wt. % (one grain belonging to harzburgite MGP1d with 0.72 wt. %)] and higher SiO_2 contents (55.8-57.1 wt. %). Opx from the other two harzburgites (MGP1b and MGP1g) have Al_2O_3 (2.30-3.32 wt. %) contents comparable (or slightly higher) than those of lherzolites but they have lower mg#, ranging from 84.2 to 88.7. They are also marked by similar CaO contents (0.79-0.98 wt. %) but lower SiO_2 (54.1-55.9 wt. %) and Cr_2O_3 (0.26-0.60 wt. %) contents. Finally opx from the harzburgites MGP4b are characterized by a very high mg# (91.6-93.0), and by Al_2O_3 (2.38-2.94 wt. %,), SiO_2 (55.8-57.2 wt. %) and CaO (0.85-1.00 wt. %) similar to those of lherzolites. Cr_2O_3 content is slightly higher, ranging from 0.44 to 0.73 wt. %.

Opx3 (those arranged in vein in the dunite MGP2a) are always distinguished from the other two kinds of opx. Mg# is analogous to those of opx from lherzolites and harzburgites MGP1c and MGP3b, comprised between 89.2 and 90.6, but, at comparable mg#, they have (higher Al_2O_3 (3.02-3.52 wt. %), and lower CaO (0.76-0.89 wt. %), SiO_2 (54.0-55.5 wt. %) and Cr_2O_3 (0.20-0.40 wt. %) contents. Opx1 from the other dunitic sample (MGP1h) have similar Cr_2O_3 (comprised in the range 0.25-0.42 wt. %, except one analyses, up to 0.56 wt. %) and CaO (0.80-0.96 wt. %) contents to those of opx3 of dunite MGP2a, but this latter one shows higher SiO_2 (57.3-57.9 wt. %) and lower Al_2O_3 (1.18-1.59 wt. %) contents.

6.1.4. Spinel

On the basis of their petrolographic and textural features, sp have been classified in two groups: those occurring with cpx (sp_{cpx}) and those not related to pyroxene (sp). The first group is composed solely of sp_{cpx} that have higher Al_2O_3 content with respect to Cr_2O_3 (mg# ranging from 61.2 to 77.2 and cr# between 37.1 and 51.0). The other sp group can be characterized by higher cr# (49.2-60.6) and mg# comprised between 62.0 and 67.4. A few grains of both sp and sp_{cpx} plot outside these two groups, at very low cr# (17.5-26.5) and mg# (55.0-64.9).

Taking into account the lithotype, sp from lherzolites have mg# and cr# ranging from 72.3 to 73.1, and from 37.1 to 38.2 respectively, with only one grain of sample MGP2b2 falling outside these ranges (mg#=77.2 and cr#=38.5) (**Table 5**). Those belonging to harzburgites have a quite different geochemical composition, with one sample (MGP4b) having the highest mg# (74.8-76.9) and cr# (38.3-40.5) similar to that of lherzolites; three harzburgites (MGP1b, MGP1c and MGP3b) are characterized by higher cr# with respect to harzburgite MGP4b and two lherzolites (42.6-60.0) and lower mg# (61.2-67.5), and two sp of harzburgite MGP1g with a very low mg# and cr#. Sp of dunites fall in the field defined by the three harzburgites MGP1b, MGP1c and MGP3b, with mg# ranging from 62.0 to 66.4 and cr# from 46.6 to 57.1. Three sp_{cpx} from dunite MGP1h plot outside this group, having slightly higher mg# (69.6-70.4) and lower cr# (43.5-43.9). Finally sp of the wehrlite are the most aluminiferous (cr# 17.5-20.8) with mg# ranging from 62.6 to 64.9.

6.2. Trace elements

6.2.1. Clinopyroxene

Chondrite-normalized (*Sun and McDonough, 1989*) trace elements and rare earth element (REE) compositions for each sample are reported in **Fig. 7** and **Table 6**. No correlation between composition and textural position and/or the lithotype have been observed for cpx1 and cpx2. They are practically indistinguishable solely on the basis of trace element composition.

Cpx from lherzolites are characterized by a remarkable Th positive anomaly, a strong Nb and less pronounced Zr and Ti negative anomalies. Most of them are light REE (LREE) enriched with $(La/Yb)_N$ ranging from 2.09 to 5.57. A few grains are characterized by a lower $(La/Yb)_N$ ratio comprised between 1.55 and 1.96, related to an increase of the heavy REE (HREE) content. Cpx from harzburgites show anomalies similar to those highlighted for the lherzolites. With respect to these latter they are characterized by a more pronounced negative Ti anomaly and by a variable, but always negative, Zr anomaly. Harzburgite MGP1c (and a few grains of MGP4b) show a slightly negative Zr anomaly, whereas cpx from harzburgites MGP1b, MGP3b and MGP4b are marked by a strong negative Zr anomaly. The REE patterns resemble those of the lherzolites, with an enrichment in LREE, most of the cpx having a $(La/Yb)_N$ comprised between 2.09 and 7.28. As for lherzolites, some cpx in harzburgites are characterized by HREE enrichment, leading to a decrease of the $(La/Yb)_N$ ratio (0.87-1.68).

Only one cpx crystal was found and analysed in dunite MGP2a. It shows a more fractionated incompatible trace element pattern, always characterized by the prominent positive Th and negative Nb anomalies. It also has marked Zr and Ti negative anomalies, and a steep REE pattern, with a $(La/Yb)_N$ equal to 4.11.

Cpx of the wehrlite are also characterized by negative Nb and positive Th anomalies, even if the latter is less marked than that of the other cpx. Indeed, in lherzolites Th content varies from 0.24 up to 14.7 ppm, in the harzburgites from 0.71 to 14.2 ppm, in the dunite it is equal to 2 ppm, whereas in wehrlite it ranges from 0.12 and 0.41 ppm. The two negative Zr and Ti anomalies are present in the wehrlitic clinopyroxenes, the former anomaly being generally marked and the second varying from slight to strong. REE patterns highlight two different compositions, one with a convex upward pattern and a $(La/Yb)_N$ ranging from 0.79 and 1.04 and the other with LREE enrichment and a $(La/Yb)_N$ varying from 2.87 up to 5.26. These two compositions, however, are not related to different textural position.

6.2.2. Orthopyroxene

Chondrite-normalized (*Sun and McDonough, 1989*) trace elements profiles and REE of opx are reported in **Fig 8** and **Table 7**. Lherzolites are characterized by a prominent positive Th and negative Sr, Zr and Ti anomalies. They also show depleted LREE with a negative Ce anomaly and HREE at about 5X chondritic, with $(La/Yb)_N$ ratios varying between 0.06 and 0.30.

Opx from harzburgites MGP1b and MGP1c display the same anomalies observed for the lherzolites, i.e. positive Th and negative Sr, Zr and Ti anomalies as well as flat HREE with a drastic LREE depletion resulting in a $(La/Yb)_N$ ratio ranging from 0.14 to 0.74. The other three harzburgites (MGP1g, MGP3b and MGP4b) are characterized by the same strong positive Th and negative Sr anomalies but slightly negative Zr and Ti anomalies. The REE patterns show flat HREE and depleted LREE, with $(La/Yb)_N$ ranging from 0.16 and 0.74.

Opx analysed in the two dunites MGP1h and MGP2a always show marked positive Th and negative Sr anomalies, but the former has slightly negative Zr and Ti anomalies, the latter (opx3 in vein) displays a positive Zr and a prominent negative Ti anomaly. The REE patterns are similar to those described above, with flat HREE and a depletion in LREE also resulting in this case in the low $(La/Yb)_N$ ratio, between 0.21 and 0.36. Considering the different REE patterns and the negative Ti anomaly, Ti* $[Ti_N/((Eu_N+Gd_N)/2)]$ is plotted versus $(Ce/Yb)_N$, highlighting the presence of two groups of opx, one at low Ti* (i.e. prominent Ti negative anomaly) and $(Ce/Yb)_N$ and one at higher values of both $(Ce/Yb)_N$ and Ti* (**Fig. 9A**). **Fig. 9B** better constrains this subdivision by taking into account the Zr negative anomaly (Zr*, $[Zr_N /((Sm_N +Nd_N)/2)]$) which varies from slight to prominent, but also positive in one case. Moreover it allows distinguishing a third group constituted by the opx in the vein of sample MGP2a that clearly plots outside Group II due to its positive Zr anomaly.

7. P-T conditions and *f*O₂.

Temperature and Pressure conditions were estimated using the two-pyroxene thermometer of *Brey and Kölher (1990)* and the *Kölher and Brey (1990)* barometer, this latter one based on the Ca exchange between ol and cpx. Temperature has been estimated on lamellae-free opx. Some care is needed regarding the pressure estimates because the Ca content of the ol has only been measured by electron microprobe. Beside some unreasonably high (>30 Kb) and low (<5 Kb) pressure values, most of the samples fall in the spinel stability field (P ranging from 12 to 20 Kb) within a narrow range of temperature (1003 ºC – 1040 ºC).

Temperature estimates for ESM compare favourably to the upper ranges of estimates from other Central Patagonia localities. *Bjerg et al. (2005)* calculated at Gobernador Gregores equilibration temperatures for spinel peridotites ranging from 830 ºC to 1090 ºC; *Dantas (2007)* reports temperatures from 850 ºC to 1100 ºC for the same locality. Temperatures of spinel lherzolites from Tres Lagos range between 728 ºC and 1040 ºC (*Ntaflos et al., 2006*), while *Faccini et al. (2013)* calculates temperatures between 872 ºC and 1006 ºC at Cerro Fraile.

$\Delta \log fO_2$ (QFM) have been calculated using the equilibrium of the ol-sp-opx assemblage according to *Ballhaus et al. (1991)* (**Fig. 10**). Pressure used for the oxygen fugacity is 15 Kbar, while temperatures, varying between 912 ºC and 980 ºC, are in good agreement with those calculated with the *Brey and Kölher (1990)* thermometer (**Table 8**). All samples have positive $\Delta \log fO_2$ indicating oxidized conditions. The two lherzolites have the lowest values (+0.02 and +0.62) while the harzburgites have values higher than +1, with the most oxidized samples reaching +1.47. The mean value of the fO_2 is +0.86, slightly higher than that calculated for supra-subduction mantle xenoliths (+0.51, *Foley, 2011*). The oxygen fugacity calculated at ESM is quite different from that calculated at Cerro del Fraile. For this locality, an average $\Delta \log fO_2$ of -0.41 and -0.34 were calculated by *Faccini et al. (2013)* and *Wang et al. (2007)* respectively.

8. Discussion

8.1. Depletion processes

Partial melting of ESM mantle xenoliths has been estimated using trace (*Johnson et al., 1990)* and major element (*Bonadiman et al., 2011)* modelling, the former based on the HREE content in cpx and the second on the Al_2O_3 content in cpx and opx.

It is well known that HREE in peridotites are very sensitive to the partial melting degree (*F*), i.e. an increase of *F* corresponds to a decrease of HREE in the residue. Contrary to LREE, HREE values are also less affected by successive enrichment due to metasomatism. In **Fig. 11A** and **B** the melting curves for REE (with Zr, Ti and Y) are reported according to the equations of *Johnson et al. (1990)*, starting from a Primitive Mantle (PM) composition from *Bonadiman et al. (2005)* and assuming a modal composition of 55% ol, 22% opx, 20% cpx and 3% sp, at 1.5 GPa. Cpx HREE contents in lherzolites suggest an *F* between ~ 5% and ~ 13% (**Fig.11A**); cpx from harzburgite MGP3b and few cpx from MGP4b fall in the range of *F* comprised between ~ 5% and ~ 15% (**Fig. 11B**). The cpx of the other harzburgites (MGP1b and MGP1c) have HREE equal or higher than PM and for this reason they do not lead to any result.

The melting history of the ESM mantle is also provided by the Al_2O_3 variation for cpx and opx, according to the melting trends of *Bonadiman et al. (2011)* (**Fig. 12**). Al_2O_3 behavior is strictly related to partial melting processes in basaltic systems, i.e. the increasing of melting results in a decreasing of the Al_2O_3 in opx, cpx and sp, and for this reason it can be chosen as a robust geochemical parameter when dealing with partial melting modelling (*Ionov and Hofmann, 2007*; *Bonadiman et al., 2011*). In the Al_2O_3 vs. MgO diagram (**Fig. 12A** and **B**) an *F* comprised between ~ 15% and ~ 30% for the opx (**Fig. 12A**) and between ~ 16% and ~ 23% for cpx (**Fig. 12B**) is indicated, with opx being more scattered than cpx.

Opx from the two lherzolites record the same degree of melting (*F* ~ 20%) while the cpx spans from ~ 16% to 20%. Opx from harzburgites are distributed quite well along the partial melting line in both cases, even if those from MGP1c tend to diverge towards lower and higher values of MgO and Al_2O_3 respectively and those of MGP4b towards higher values of both oxides. In this case the estimated *F* ranges from ~ 20% to ~ 30%. On the contrary, cpx of harzburgites are well aligned on the curve, recording an *F* between ~ 16% and ~ 23%. Cpx from dunites are slightly scattered towards lower Al_2O_3 values aligning along a partial melting curve parallel to that of *Bonadiman et al. (2011)* with *F* similar to that of the cpx from harzburgites ranging from ~ 16% to ~ 23%. Opx from MGP2a recording an *F* similar to that of the lherzolites (~ 16%) should not be considered because it is arranged in vein and it clearly postdates the partial melting event(s).

To summarize, HREE modelling of cpx from lherzolites record an *F* varying between ~ 5% and ~ 13%. The highest values (F ranging from ~ 16% and ~ 23%.) obtained through the Al_2O_3 model are probably too high to be reliable, also taking into account the fact that the cpx modal content of this lithotype varies from 9.5% (MGP2b) to 13.3% (MGP2b2). On the other hand, HREE content of cpx from harzburgites MGP3b and MGP4b record an *F* comprised between ~ 5% and ~ 15%. In this case the highest values (*F* comprised between ~ 20% and ~ 30%.) obtained by the major element modelling are compatible with the modal composition of 73% ol, 21% opx, 4% cpx and 2% sp.

8.2. Enrichment processes and nature of the incoming melt(s)

Cpx and opx of ESM are characterized by a decrease in Al_2O_3 content related to an increase in mg# (**Fig. 6A** and **B**). Furthermore a correlation between the increase of the mg# and the nature of the lithotype, i.e. the modal content of cpx left after the partial melting (a gradual shift from lherzolites to harzburgites to dunites) is not observed. An evolution of the mantle beneath ESM linked only to a partial melting event is also ruled out by the negative correlation between major (in terms of Al_2O_3 contents) and trace element compositions (namely LREE and Sr, **Fig. 13A** and **B**). A residue after partial melting in fact would have minor Al_2O_3 content coupled with a decrease in LREE (i.e. a decrease of the La/Yb ratio) and Sr (i.e. a positive correlation), contrary to what was observed at ESM. These geochemical features, together with the petrographic evidence of two texturally different cpx and the presence of a vein of recrystallized opx, highlight the occurrence of possible metasomatic and/or refertilization events affecting the upper mantle beneath ESM.
The main problem when dealing with metasomatism/refertilization events is the identification of the liquid percolating through the mantle thereby modifying its geochemical features. In order to constrain the nature of the melt, we compared the incompatible trace elements and REE patterns of the ESM cpx with those of pyroxenites and wehrlites from northern and central Patagonia (*Dantas, 2007*) (**Fig. 14A-F**). Four main processes are accounted for the generation of pyroxenites. Various authors consider them

as (1) formed by oceanic crust recycling (*Polvé & Allègre, 1980; Allègre & Turcotte, 1986; Kornprobst et al., 1990; Kerr et al., 1995*), or (2) as cumulus at the base of the magmatic chamber (*DeBari & Coleman, 1989; Schiano et al., 2000*), as well as (3) segregated at high pressure from mafic silicate liquids (*Downes, 2005*) or (4) as products of the interaction between the peridotite with melts at mantle depth, suggesting the presence of refertilization/metasomatic event(s) (*Kelemen et al., 1992*; *Smith & Riter, 1997*; *Wilkinson & Stolz, 1997*; *Garrido & Bodinier, 1999*; *Smith et al., 1999*; *Zanetti et al., 1999*; *McInnes et al., 2001*; *Wang et al., 2001*). In this case, the samples are porphyroclastic to equigranular opx-rich websterites from Cerro Rio Chubut and Cerro Aznare (**Fig. 1**, Northern Patagonia), as well as porphyroclastic to equigranular olivine and spinel websterites from Cerro de Los Chenques (**Fig. 1**, Northern Patagonia), and porphyroclastic spinel clinopyroxenites from Cerro Clark (**Fig. 1**, Central Patagonia).

The first group of pyroxenites from Northern Patagonia is characterized by prominent Nb and slightly negative Ti anomalies, depleted LREE and enriched-to-flat HREE (***Trend 1*, Fig.14A** and **B**). The same feature can also be observed for the cpx of the pyroxenites from central Patagonia that fall in the same group, except for a slightly negative Zr anomaly and for less enriched REE patterns. Wehrlites from central Patagonia show the highest trace element concentrations, with prominent negative Nb and Ti anomalies, a negative to positive Zr anomaly, enriched LREE and fractionated HREE (***Trend 2*, Fig.14C** and **D**). Finally, a second group of cpx of pyroxenites from northern Patagonia is characterized by a wider range of trace element concentrations, with negative Nb, Zr and Ti anomalies. LREE contents vary from depleted to slightly enriched and fractionated to flat HREE (***Trend 3*, Fig.14E** and **F**). The grey field in **Fig. 14,** corresponding to the ESM cpx, resembles the pattern of cpx of ***Trend 3***.

To constrain the origin of ***Trend 1***, the REE patterns of cpx belonging to the pyroxenites of Northern and Central Patagonia have been compared to those of cpx phenocrysts from tholeiitic lavas from Ethiopian Rift (*Beccaluva et al., 2009*) (**Fig. 15**). To the best of our knowledge no trace element analyses are available on cpx phenocrysts from Patagonian lavas. The overlap between cpx in equilibrium and Ethiopian tholeiitic lavas is quite remarkable. This fact lends support to the percolation of sub-alkaline SiO_2 – saturated melt beneath Northern and Central Patagonia. In the main plateau –

post-plateau (and in some cases also pre-plateau) eruption sequence typical of the Somoncura and Triple Junction mesetas, tholeiitic products are predominant especially in the voluminous main plateau volcanic stage. It is thus likely that the northern and central Patagonian mantle suffered tholeiitic refertilization processes, characterized by a much higher melt/rock ratio with respect to a metasomatic event.

The cpx REE patterns of wehrlites belonging to ***Trend 2*** appear enriched in LREE with a La/Lu ranging from 6.89 to 30.5 and a high content of Nb, Sr and Zr. These resemble typical patterns for mineral crystallized from alkaline melts. According to Dantas (2007) these patterns are, in fact attributed to CaO-rich SiO_2-undersaturated melt.

Incompatible trace elements and REE patterns of ESM cpx resemble those of pyroxenites from Northern Patagonia generating ***Trend 3*** (**Fig. 14E** and **F**). The pattern of the cpx in equilibrium with the transitional/alkaline lavas from the post-plateau stage of these provinces were calculated using the appropriate partition coefficient (data from GERM, http://earthref.org/GERM/, provided as a supplementary table) and considering the most and the least enriched lavas belonging to the Triple Junction Province. As can be seen in **Fig. 16** cpx calculated (provided as supplementary data) in equilibrium with the transitional/alkaline lavas from TJ province have patterns that are quite comparable with those of the cpx from Northern Patagonia pyroxenites (***Trend 3***) and from ESM. This is also supported by a favourable comparison between La/Yb ratios of cpx from ESM (comprised between 0.87 and 7.28), those of cpx from pyroxenites (between 0.26 and 6.95) and those of the calculated cpx (between 0.57 and 6.44).

This supports the idea that a transitional alkaline/subalkaline melt refertilization event has affected the mantle beneath ESM, as also suggested by the textural features represented by cpx2 and opx in vein. A few samples show an incongruent Al_2O_3 behavior between opx and cpx (**Fig. 6**) that can be explained by an incomplete refertilization process. In fact cpx2 and opx3 tend to be enriched in Al_2O_3 with respect to the cpx1 and opx1. This, together with the presence of small vein of opx, would point toward a process occurring in recent time, just prior to xenolith entrainment.

It is to be pointed out that, while migrating through the mantle, transitional-type basalts can easily move above and below the saturation threshold. Reaction and dissolution of opx would in fact increase the SiO_2-saturation level, while its crystallization as completely new minerals or in substitution of ol would decrease it (*Arai et al., 2006*) Within this framework we can place the slightly different, more alkaline, pattern of the cpx in dunite MGP2a, as well as the presence of small opx in vein suggesting a SiO_2-rich melt. Whether or not these affinities represent truly distinct families of melts or simple, small volume variations of a unique transitional melt will be the topic of a forthcoming paper taking into consideration the metasomatic/refertilization petrological modifications of the entire Patagonia (*Melchiorre et al.,* in prep.)

9. Conclusions

Anhydrous spinel-bearing peridotites (mainly harzburgites and dunites, with minor lherzolites and one wehrlite) sampled at ESM (Patagonia), without any evidence of spongy rims or glassy patches, show two and three texturally different cpx and opx, respectively. They depict two different trends, one characterized by high Al_2O_3 content at almost constant mg# and the second by a slight increase of the Al_2O_3 content with a decreasing of mg#. The trace element concentrations do not evidence any difference between cpx1 and cpx2, but discriminate three groups of opx, in agreement with the observed petrographical features: one is represented by the opx3 (those arranged in vein) characterized by a prominent positive Zr anomaly, while the other two always show prominent-to-slightly negative Ti and Zr anomalies and LREE depleted patterns.

Equilibration temperature estimates of ESM peridotites range from 1003 ºC and 1040 ºC, comparing favourably to the upper ranges of estimates from other Central Patagonia localities. Positive $\Delta \log fO_2$ (QFM, average of +0.86) is compatible with that calculated for a supra-subductive mantle by *Foley (2001)* (+0.51), revealing an oxidizing environment, on the contrary of what was proposed by *Wang et al (2007)* and *Faccini et al. (2013)* at Cerro del Fraile (-0.34 and -0.41 respectively). Major and trace element modelling of partial melting reveals an *F* ranging from ~ 5% and ~ 13% for the lherzolites and between ~ 20% and ~ 30% for the harzburgites.

The correlation between incompatible trace elements [$(La/Yb)_N$ and Sr_N] and Al_2O_3 of the cpx highlight the presence of a refertilization event affecting the ESM upper mantle, evidenced by the enrichment of the LREE and Sr correlated to a decrease in the Al_2O_3 content. The agent that can account for this process has a transitional affinity and is analogous to the lavas occurring within the various post-plateau stages of the mesetas belonging to the Triple Junction Province. This conclusion has been reached by reconstructing the REE patterns of a cpx in equilibrium with lavas with the lowest and highest trace element contents from this province that resemble those of the cpx from ESM.

Acknowledgements

This work is part of a co-tutorship Ph.D. held within the 2008 Vinci Project "Matter transfer in supra-subductive mantle in complex converging systems" funded by the "Università Italo-Francese". The activities have been carried out between the University of Ferrara and the CNRS of Toulouse. We thank the laboratory staff of UMR 5563 (LMTG, Observatoire Midi-Pyrenees) for their support during the performance of EMP and LA-ICP-MS analysis. We also thank Renzo Tassinari (University of Ferrara) for the XRF analysis and Grant George Buffett (Institute of Earth Science Jaume Almera – CSIC of Barcelona) for English editing. We thank Theodoros Ntaflos, Csaba Szabo and Sonja Aulbach for their revisions. Their constructive comments have largely improved the first version of the manuscript.

10. References

Allègre, C. J., Turcotte, D. L., 1986. Implications of a two-component marble-cake mantle. Nature 323, 123-127.

Aoki, K., 1987. Japanese Island arc: xenoliths in alkali basalts, high-alumina basalts, and calc alkaline andesites and dacites, in P. H. Nixon (Ed), Mantle Xenoliths. John Wiley & Sons, New York, 319–33.

Arai, S., Hirai, H., ABE, N., 1998. Petrological characteristics of the sub-arc mantle: An overview on petrology of peridotite xenoliths from the Japan arc. Trends in Mineralogy (India) 2, 39–55.

Arai, S., Ishimaru, S., Okrugin, V. M., 2003. Metasomatized harzburgite xenoliths from Avacha volcano as fragments of mantle wedge of the Kamchatka arc: an implication for the metasomatic agent. Island Arc 12, 233-246.

Arai, S., Shimizu, Y., Morishita, T., Ishida, Y., 2006. A new type of orthopyroxenite xenolith from Takashima, Southwest Japan: silica enrichment of the mantle by evolved alkali basalt. Contribution to Mineralogy and Petrology 152, 387-398.

Ardolino, A., Franchi, M., Remesal, M., Salini, F., 1999. El volcanismo en la Patagonia extrandina, in: R. Caminos (Ed), Geologia Argentina. Servicio Geologico Nacional Anales 29, 579–612.

Bali, E., Zajacz, Z., Kovács, I., Szabó, CS., Halter, W., Vaselli, O., Török, K., Bodnar, R. J., 2008. A quartz-bearing orthopyroxene-rich websterite xenoliths from the Pannonian Basin, Western Hungary: evidence for release of quartz-saturated melts from a subducted slab. Journal of Petrology 49, 421-439.

Ballhaus, C., Berry, R. F., Green, D. H., 1991. High pressure experiment calibration of the olivine-orthopyroxene-spinel oxygen barometer: implications for the oxidation state of the mantle. Contributions to Mineralogy and Petrology 107, 27-40.

Beccaluva, L., Bianchini, G., Natali, C., Siena, F., 2009. Continental flood basalts and mantle plume: a case study of the Northern Ethiopian Plateau. Journal of Petrology 50, 1377-1403.

Berkesi, M., Guzmics, T., Szabó, C., Dubessy, J., Bodnar, R. J., Hidas, K., Ratter, K., 2012. The role of CO_2-rich fluids in trace element transport and metasomatism in the lithospheric mantle beneath the Central Pannonian Basin, Hungary, based on fluid inclusions in mantle xenoliths. Earth and Planetary Science Letters 331-332, 8-20.

Bianchini, G., Beccaluva, L., Nowell, G.M., Pearson, D.G., Siena, F., 2011. Mantle xenoliths from Tallante (Betic Cordillera): insights into the multi-stage evolution of the south Iberian lithosphere. Lithos 124, 308-318.

Bjerg, E. A., Ntaflos, T., Kurat, G., Dobosi, G., Labudía, C. H., 2005. The upper mantle beneath Patagonia, Argentina, documented by xenoliths from alkali basalts. Journal of South American Earth Sciences 18, 125-145.

Bonadiman, C., Beccaluva, L., Coltorti, M., Siena, F., 2005. Kimberlite-like metasomatism and 'garnet signature' in spinel peridotite xenoliths from Sal, Cape Verde Archipelago: relics of a subcontinental mantle domain within the Atlantic Oceanic lithosphere? Journal of Petrology 46, 2465-2493.

Bonadiman, C., Coltorti, M., Beccaluva, L., Griffin, W. L., O'Reilly, S.Y., Siena, F., 2011. Metasomatism vs host magma infiltration: a case study of Sal mantle xenoliths, Cape Verde Archipelago. In: Coltorti, M. & Gregoire, M. (eds) Metasomatism in Oceanic and Continental Lithospheric Mantle. Geological Society of America, Special Papers 478, 283-305.

Brey, G. P., Köhler, T., 1990. Geothermobarometry in four-phase lherzolites II. New thermobarometers and practical assessment of existing thermobarometer. Journal of Petrology 31, 1353-1378.Cande, S.C., Leslie, R.B., 1986. Late Cenozoic tectonics of the Southern Chile Trench. Journal of Geophysical Research 91, 471-496.

Coltorti, M., Bonadiman, C., Faccini, B., Gregoire, M., O'Reilly, S. Y., Powell, W., 2007. Amphiboles from suprasubduction and intraplate lithospheric mantle. Lithos 99, 68-84.

Corbella, H., Chelotti, L., Pomposiello, C., 1996. Neotectonica del rift Jurasico austral en Pali Aike, Patagonia Extrandina, Santa Cruz, Argentina. In: XIII Congreso Geologico Argentino y III Congreso de Exploracion de Hidrocarburos, Actas II, 383–393.

D'Orazio M., Agostini S., Mazzarini F., Innocenti F., Manetti P., Haller M., Lahsen A., 2000. The Pali Aike Volcanic Field, Patagonia: slab-window magmatism near the tip of South America. Tectonophysics 321, 407-427.

D'Orazio M., Agostini S., Innocenti F., Haller M., Manetti P., Mazzarini F., 2001. Slab window-related magmatism from southernmost South America: the Late Miocene mafic volcanics from the Estancia Glencross Area (~52°S, Argentina–Chile).

Dantas, C., 2007. Caractérisation du manteau supérieur patagonien: les enclaves ultramafiques et mafiques dans les laves alcalines. PhD thesis.

DeBari, S. M., Coleman, R. J., 1989. Examination of the deep levels of an island arc: evidence from the Tonsina ultramafic–mafic assemblage. Journal of Geophysical Research 94, 4373–4391.Diraison, M., Coppold, P.R., Gapais, D., Rossello, E.A., 1997. Magellan Strait: part of a Neogene rift system. Geology 25, 703–706.

Downes, H., 2005. Geochemical constraints on the origin of mantle pyroxenites. American Geophysical Union, V41E-1505.Faccini, B., Bonadiman, C., Coltorti, C., Gregoire, M., Siena, F., 2013. Oceanic Material Recycled within the Sub-Patagonian Lithospheric Mantle (Cerro del Fraile, Argentina). Journal of Petrology 54, 1211-1258.

Foley, S. F., 2011. A reappraisal of redox melting in the Earth's mantle as a function of tectonic setting and time. Journal of Petrology 52, 1363-1391.

Forsythe, R., Nelson, E., Carr, M.J., Keading, M.E., He& M., Mpodozis, C., Soffia, J.M. and Harambour, S., 1986. Pliocene near trench magmatism in Southern Chile: a possible manifestation of ridge collision. Geology, 14: 23-27.

Franz, L., Becker, K. P., Kramer, W., Herzig, P. M., 2002. Metasomatic mantle xenoliths from the Bismark microplate (Papua New Guinea) - thermal evolution, geochemistry and extent of slab-induced metasomatism. Journal of Petrology 43, 315-343.

Garrido, C. J., Bodinier, J. L., 1999. Diversity of mafic rocks in the Ronda peridotite: evidence for pervasive melt–rock reaction during heating of subcontinental lithosphere by upwelling asthenosphere. Journal of Petrology 40, 729-754.

Gorring, M. L., Kay, S. M., Zeitler, P. K.,Ramos, V. A., Rubiolo, D., Fernandez, M. I., Panza, J. L., 1997. Neogene patagonian plateau lavas: continental magmas associated with ridge collision at the Chile Triple Junction. Tectonics 16, 1-17.

Gorring, M.L., Kay, S.M., 2000. Carbonatite metasomatized peridotites xenoliths from southern Patagonia: implications for lithospheric processes and Neogene plateau magmatism. Contribution to Mineralogy and Petrology 140, 55–72.

Gorring, M. L., Kay, S. M., 2001. Mantle processes and sources of Neogene slab window magmas from Southern Patagonia, Argentina. Journal of Petrology 42, 1067-1094.

Gorring, M. L., Singer, B., Gowers, J., Kay, D. M., 2003. Plio-Pleistocene basalts from the Meseta del Lago Buenos Aires, Argentina: evidence for asthenosphere-lithosphere interactions during slab window magmatism. Chemical Geology 193, 215-235.

Green, D. H., Edgar, A. D., Beasley, P., Kiss, E., Ware, N. G., 1974. Upper mantle source for some hawaiites mugearites and benmoreites. Contribution to mineralogy and Petrology 48, 33-44.

Hidas, K., Guzmics, T., Szabó, CS., Kovács, I., Bodnar, R. J., Zajacz, Z., Nédli, Z., Vaccari, L., Perucchi, A., 2010. Coexisting silicate melt inclusions and H_2O-bearing, CO_2-rich fluid inclusions in mantle peridotite xenoliths from the Carpathian-Pannonian region (central Hungary). Chemical Geology 274, 1-18.

Ionov, D. A., Hofmann, A.W., 2007. Depth of formation of subcontinental off-craton peridotites. Earth and Planetary Science Letters 261, 620-634.

Ionov, D. A., Seitz, H. M., 2008. Lithium abundances and isotopic compositions in mantle xenoliths from subduction and intra-plate settings: mantle sources versus eruption histories. Earth and Planetary Science Letters 266, 316-331.

Johnson, K. T. M., Dick, H. J. B., Shimizu, N., 1990. Melting in the oceanic upper mantle: an ion microprobe study of diopsides in abyssal peridotites. Journal of Geophysical Research 95, 2661-2678.

Kay, S. M., Ramos, V. A., Mpodozis, C., Sruoga, P., 1989. Late Paleozoic to Jurassic silicic magmatism at the Gondwanaland margin: analogy to the Middle Proterozoic in North America? Geology 17, 324–328.

Kay, S.M., Ramos, V.A., Marquez, M., 1993. Evidence in Cerro Pampa volcanic rocks for slab-melting prior to ridge-collision in southern South America. Journal of Geology 101, 703- 714.

Kay, S. M., Ardolino, A., Gorring, M. L., Ramos, V. A., 2007. The Somoncura large igneous province in Patagonia: interaction of a trancient mantle thermal anomaly with a subducting slab. Journal of Petrology 48, 43-77.

Kelemen, P. B., Dick, H. J. B., Quick, J. E., 1992. Formation of harzburgite by pervasive melt/rock reaction in the upper mantle. Nature 358, 635-641.

Kempton, P.D., Hawkesworth, C.J., Lopez-Escobar, L., Pearson, D.G., Ware, A.J., 1999. Spinel±garnet lherzolite xenoliths from Pali Aike: Part 2. In: Gurney, J.J., Gurney, J.L., Pascoe, M.D., Richardson, S.H. (Eds.), Trace element and isotopic evidence bearing on the evolution of lithospheric mantle beneath southern Patagonia. The J.B. Dawson Volume. Proc. International Kimberlite Conference 7, vol. 1, 415–428.

Kepezhinskas, P. K., Defant, M. J., Drummond, M. S., 1995. Na metasomatism in the island-arc mantle by slab melt-peridotite interaction: evidence from mantle xenoliths in the north Kamchatka arc. Journal of Petrology 36, 1505-1527.

Kerr, A. C., Saunders, A. D., Tarney, A. D., Berry, N. H., Hards, V. L., 1995. Depleted mantle plume geochemical signatures: no paradox for plume theories. Geology 23, 843-846.

Kilian, R., Franzen, C., Koch, M., 1998. The metasomatism of the mantle wedge below the southern Andes: constraints from laser ablation microprobe ICP-MS trace element analysis of clinopyroxenes, orthopyroxenes and fluid inclusions of mantle xenoliths. Terra Nostra 98/5, 81–82.

Kilian, R., Stern, C.R., 2002. Constraints on the interaction between slab melts and the mantle wedge from adakitic glass in peridote xenoliths. European Journal of Mineralogy 14, 25–36.

Köhler, T., Brey, G. P., 1990. Ca-exchange between olivine and clinopyroxene as a geothermobarometer calibrated from 2 to 60 kbar in primitive natural lherzolites. Geochimica et Cosmochimica acta 54, 2375-2388

Koloskov, A.V., Khotin, M.YU., 1978. Ultramafic inclusions in lavas of present Kamchatka volcanoes, in: Academy of Sciences of the USSR Soviet Geophysical Committee (Eds), Inclusions in the Volcanic Rocks of the Kuril-Kamchatka Island Arc, Nauka, Moscow (in Russian with English abstract), pp. 36–66.

Kornprobst, J., Piboule, M., Roden, M., Tabit, A., 1990. Corundum-bearing garnet clinopyroxenites at Beni Bousera (Morroco): original plagioclase-rich gabbros recrystallized at depth within mantle. Journal of Petrology 31, 17-45.

Kurat, G., Palme, H., Spettel, B., Baddenhausen, H., Hofmeister, H., Palme, C., Wanke, H., 1980. Geochemistry of ultramafic xenoliths from Kapfenstein, Austria: evidence for a variety of upper mantle processes. Geochimica et Cosmochimica Acta 44, 45-60.

Lachance, G.R., Traill, R.J., 1966. Practical solution to the matrix problem in X-ray analysis. Canadian Spectroscopy 11, 43-48.

Laurora, A., Mazzucchelli, M., Rivalenti, G., Vannucci, R., Zanetti, A., Barbieri, M.A., Cingolani, C.A., 2001. Metasomatism and melting in carbonated peridotite xenoliths from the mantle wedge: the Gobernador Gregores case (Southern Patagonia). Journal of Petrology 42, 69–87.

Le Bas, M. J., Streckeisen, A. L., 1991. The IUGS systematics of igneous rocks. Journal of the Geological Society, London, 148, 825-833.

McDonough,W. F., Sun, S., 1995. The composition of the Earth. Chemical Geology 120, 223-253.

McInnes, B. I. A., Gregoire, M., Binns, R. A., Herzig, P. M., Hannington, M. D., 2001. Hydrous metasomatism of oceanic subarc mantle, Lihir, Papua New Guinea: petrology and geochemistry of fluid-metasomatised mantle wedge xenoliths. Earth and Planetary Science Letters 188, 169-183.

Mercier, J.C., Nicolas, A., 1975. Textures and fabrics of upper mantle peridotites as illustrated by xenoliths from basalts. Journal of. Petrology 16, 454– 487.

Nixon, P. H., 1987. Mantle Xenoliths. John Wiley & Sons, New York.

Ntaflos, T., Bjerg, E. A., Labudia, C. H., Kurat, G., 2006.Depletd lithosphere from the mantle wedge beneath Tres Lagos, southern Patagonia, Argentina. Lithos 94, 46-65.

Pankhurst, R. J., Rapela, C. W., 1995. Production of Jurassic rhyolite by anatexis of the lower crust of Patagonia. Earth and Planetary Science Letters 134, 223–236.

Polvé, M., Allègre, C. J., 1980. Orogenic lherzolite complexes studied by 87Rb-87Sr: A clue to understand the mantle convection processes? Earth and Planetary Science Letters 51, 71-93.

Pouchou, J. L., Pichoir, F. 1984. A new model for quantitative X-ray microanalysis. Part 1: application to the analysis of homogeneous samples. Recherche Aérospatiale 5, 13–38.

Ramos, V.A., Kay, S.M., 1992. Southern Patagonia plateau basalts and deformation: backarc testimony of ridge collisions. Tectonophysics 205, 261–282.

Rapela, C. W., Spalletti, L. A., Merodio, J. C., Aragon, E., 1988. Temporal evolution and spatial variation of lower Tertiary volcanism in the Patagonian Andes (40°–42°30'S). Journal of South American Earth Sciences 1, 75–88.

Rapela, C. W.,Kay, S. M., 1988. Late Paleozoic to Recent magmatic evolution of northern Patagonia. Episodes 11, 175-182.

Rivalenti, G., Mazzucchelli, M., Zanetti, A., Vannucci, R., Bollinger, C., Hemond, C., Bertotto, G. W., 2007. Xenoliths from Cerro de los Chenques (Patagonia): An example of slab-related metasomatism in the backarc lithospheric mantle. Lithos 49, 45-67

Saha, A., Basu, A. R., Jacobsen, S. B., Poreda, R. J., Yin, Q.-Z., Yogodzinski, G. M., 2005. Slab devolatilization and Os and Pb mobility in the mantle wedge of the Kamchatka arc. Earth and Planetary Science Letters 236, 182-194.

Schiano, P., Eiler, J. M., Hutcheon, I. D., Stolper, E. M., 2000. Primitive CaO-rich, silica-undersaturated melts in islands arcs: evidence for the involvement of clinopyroxene-rich lithologies in the petrogenesis of arc magmas. Geochemistry, Geophysics, Geosystems 1, doi:10.1029/1999GC000032.

Smith, D., Riter, J. C. A., 1997. Genesis and evolution of low-Al orthopyroxene in spinel peridotite xenoliths, Grand Canyon field, Arizona, USA. Contributions to Mineralogy and Petrology 127, 391-404.

Smith, D., Riter, J. C. A., Mertzman, S. A., 1999. Erratum to "water-rock interactions, orthopyroxene growth and Si-enrichment in the mantle: evidence in xenoliths from the Colorado Plateau, southwestern United States". Earth and Planetary Science Letters 167, 347-356.

Stern, C.R., Saul, S., Skewes, M.A., Futa, K., 1989. Garnet peridotites xenoliths from Pali-Aike basalts of southernmost South America. Kimberlites and related rocks. Geological Society of Australia, Special Publication 14, 735–744. Backwell, Carlton.

Stern, C.R., Killian, R., 1996. Role of the subducted slab, mantle wedge, and continental crust in the generation of adakites from the Andean Austral Volcanic Zone. Contribution to Mineralogy and Petrology 123, 263- 281.

Stern, C.R., Kilian, R., Olker, B., Hauri, E.H., Kyser, T.K., 1999. Evidence from mantle xenoliths for relatively thin (<100 km) continental lithosphere below the Phanerozoic crust of southernmost South America. Lithos 48, 217–235.

Streckeisen, A. L., 1976. Classification of the common igneous rocks by means of their chemical composition: a provisional attempt. Neues Jahrbuch für Mineralogie, Monatshefte, 1976, H. 1, 1-15.

Sun, S., McDonough, W. F.,1989. Chemical and isotopic systematics of oceanic basalts: implications for mantle composition and processes. In: Magmatism in the ocean basins, edited by Saunders, A. D., Norry, M. J., Geological Society of London, London, 313-345.

Takahashi, E., 1978. Petrologic model of the crust and upper mantle of the Japanese island arcs. Bulletin Volcanologique 41, 529–47.

Thorpe, R. S., Francis, P. W., Hamill, M., Baker, M. C. W., 1982. The Andes, in Andesite: orogenic andesits and related rocks, edited by R. S. Thorpe, 187-205, Chichester: Wiley.

Wang, J., Hattori, K. H., Kilian, R., Stern, C. R., 2007. Metasomatism of sub-arc mantle peridotites below southernmost South America: reduction of fO2 by slab-melt. Contributions to Mineralogy and Petrology 153, 607-624.

Wang, J. H., Yin, A., Harrison, T. M., Grove, M., Yuquan, Z., Guang-Hong, X., 2001. A tectonic model for Cenozoïc activities in the eastern Indo-Asian collision zone. Earth and Planetary Science Letters 188, 123-133.

Weyer, S., Ionov, D. A., 2007. Partial melting and melt percolation in the mantle: The message from Fe isotopes. Earth and Planetary Science Letters 259, 119-133.

Widom, E., Kepezhinskas, P., Defant, M. J., 2003. The nature of metasomatism in the sub-arc mantle wedge: evidence from Re/Os isotopes in Kamchatka peridotite xenoliths. Chemical Geology 196, 283-306.

Wilkinson, J. F. G., Stolz, A. J., 1997. Subcalcic clinopyroxenites and associated ultramafic xenoliths in alkali basalt near Glenn Innes, northeastern New South Wales, Australia. Contributions to Mineralogy and Petrology 127, 272-290.

Zanetti, A., Mazzucchelli, M., Rivalenti, G., Vannucci, R., 1999. The Finero phlogopiteperidotite massif: an example of subductionrelated metasomatism. Contributions to Mineralogy and Petrology 134, 107–122.

Figure caption.

Fig. 1: Sketch map of Patagonia (**A,** after *D'Orazio et al., 2000*). VG stands for "Volcanic Gap". (**a**), (**b**) and (**c**) indicate the back-arc volcanic fields respectively of Northern Patagonia, Central Patagonia and Southern Patagonia. **1** Cerro Aznare; **2** Cerro Rio Chubut; **3** Cerro de los Chenques; **4** Cerro Clark. Sketch map **B** (from *Gorring et al., 1997*) shows the occurrence of the different plateau of Central Patagonia. In grey and black are represented the main and post-plateau sequences respectively. Black star localizes sampling site of xenoliths at Estancia Sol de Mayo (ESM).

Fig. 2: Total alkali vs. silica diagram of *Le Bas and Streckeisen (1991)*. Dash dot line separates the alkaline and subalkaline domains.

Fig. 3: Chondrite normalized (*Sun and McDonough, 1989*) trace element compositions of Meseta Lago Buenos Aires (MLBA) post-plateau lavas.

Fig. 4: Ultramafic classification diagram (after *Streckeisen, 1976*) of the Estancia Sol de Mayo (ESM) mantle xenoliths. Empty symbols indicate samples studied only petrographically, while full symbols indicate those studied both petrographically and geochemically.

Fig. 5: Transmitted plane-polarized photomicrographs of representative assemblages in the Estancia Sol de Mayo (ESM) xenoliths. Ol, olivine; opx, orthopyroxene; cpx, clinopyroxene; sp, spinel. Cpx are further classified as cpx1 and cpx2. The former generally occur as protogranular in the peridotitic matrix, while the latter is observed around the sp. Opx is subdivided in opx1, opx2 and opx3: the first present as large protogranular crystals with exsolution lamellae while the second as small clean and undeformed grains without exsolution lamellae; the third occur as smaller grains arranged in vein. (**A**) Protogranular anhydrous spinel-bearing harzburgite MGP4b comprising ol, cpx1 and opx1. (**B**) Protogranular to porphyroclastic anhydrous spinel-bearing harzburgite MGP1b comprising ol, small porphyroclastic clean and undeformed grains of opx2, a cpx1 grain and a cpx2 growing around a black sp. (**C**) Vein of opx3 in dunite MGP2a. Opx3 are surrounded by a black matrix constituted by very small grains of ol, cpx and plagioclase.

Fig. 6: Al_2O_3 vs mg# of clinopyroxenes and orthopyroxenes. Diamonds refer to lherzolites, squares to harzburgites, triangles to dunites and asterisk to wehrlite. In **A**, black symbols represent cpx1 while grey symbols cpx2.

Fig. 7: Chondrite-normalized (*Sun and McDonough, 1989*) incompatible trace elements (**A**, **B**, **C**, **D**) and REE (**A'**, **B'**, **C'**, **D'**) of clinopyroxenes.

Fig. 8: Chondrite-normalized (*Sun and McDonough, 1989*) incompatible trace elements (**A**, **B**, **C**) and REE (**A'**, **B'**, **C'**) of orthopyroxenes.

Fig. 9: Ti* (calculated as $[Ti_N/((Eu_N+Gd_N)/2)]$) and Zr* (calculated as $[Zr_N/((Sm_N+Nd_N)/2)]$) vs. $(Ce/Yb)_N$ for some selected orthopyroxenes from Estancia Sol de Mayo (ESM). For symbols refer to **Fig. 6**.

Fig. 10: Oxygen fugacity [calculated as Δlog*f*O2 (QFM) (*Ballhaus et al., 1991*)] vs. temperature (from *Brey and Kölher, 1990)* of Estancia Sol de Mayo (ESM) peridotites. For comparison oxygen fugacity of Cerro del Fraile from *Wang et al. (2007)* and *Faccini et al. (2013).*

Fig. 11: Chondrite-normalized REE of cpx from Estancia Sol de Mayo (ESM, white lines) from lherzolites (**A**) and harzburgites (**B**) compared to the curves (black dashed lines) of 5%, 10%, 15%, 20%, 25% and 26% fractional partial melting (*Johnson et al., 1990*) of a starting fertile cpx (bold black line) from *Bonadiman et al. (2005)*.

Fig. 12: Al_2O_3 vs MgO melting trends from *Bonadiman et al., (2011)* for opx and cpx in Estancia Sol de Mayo (ESM) mantle xenoliths. Primitive Mantle (PM) opx and cpx composition in terms of Al_2O_3 and MgO were calculated on the basis of the primitive mantle composition of *McDonough & Sun (1995)*. Black crosses on curves indicate partial melting percentages.

Fig. 13: Variation in some selected samples of $(La/Yb)_N$ and Sr_N vs. Al_2O_3 of clinopyroxenes. A negative correlation between the two geochemical markers and the content of Al_2O_3 is highlighted. For symbols refer to **Fig. 6**.

Fig. 14: Chondrite-normalized (*Sun and McDonough, 1989*) incompatible trace elements (**A**, **C, E**) and REE patterns (B, **D**, **F**) of clinopyroxenes from pyroxenites of Nothern and Central Patagonia and wehrlites from Central Patagonia (*Dantas, 2007*). Light grey field represents the clinopyroxenes from Estancia Sol de Mayo (ESM).

Fig. 15: Chondrite-normalized (*Sun and McDonough, 1989*) incompatible trace elements of clinopyroxenes from pyroxenites of Nothern and Central Patagonia (*Dantas, 2007*) and

clinopyroxenes phenocrysts entrained in Northern Ethiopian continental flood basalts (from *Beccaluva et al., 2004*).

Fig. 16: Chondrite-normalized (*Sun and McDonough, 1989*) incompatible trace elements pattern reconstructions of clinopyroxenes from transitional/alkaline mafic lavas from the Triple Junction Province.

Table caption.

Table 1: Bulk rock major (in wt. %) and trace (in ppm) element analysis of six host lavas from Estancia Sol de Mayo (ESM). Mg# (MgO/(MgO+FeO) mol %) is calculated with Fe_2O_3=0.15*FeO (*Green et al., 1974*).

Table 2: Representative major element composition (in wt. %) of olivines of Estancia Sol de Mayo (ESM) mantle xenoliths. Ol: olivine; Fo: forsterite.

Table 3: Representative major element composition (in wt. %) of clinopyroxenes of Estancia Sol de Mayo (ESM) mantle xenoliths.

Table 4: Representative major element composition (in wt. %) of orthopyroxenes of Estancia Sol de Mayo (ESM) mantle xenoliths.

Table 5: Representative major element composition (in wt. %) of spinels of Estancia Sol de Mayo (ESM) mantle xenoliths.

Table 6: Trace element contents (ppm) of Estancia Sol de Mayo (ESM) clinopyroxenes.

Table 7: Trace element contents (ppm) of Estancia Sol de Mayo (ESM) orthopyroxenes.

Table 8: Equilibration temperature, pressure and *f*O2 estimates of Estancia Sol de Mayo (ESM) mantle xenoliths.

Table 1: Bulk rock major (in wt. %) and trace element (in ppm) analysis of six host lavas from Estancia Sol de Mayo (ESM).

Sample	MGP1	MGP2	MGP3	MGP4	MGP5	MGP6
Rock type	Basaltic trachy-andesite	Basaltic trachy-andesite	Basaltic trachy-andesite	Basaltic trachy-andesite	Basaltic trachy-andesite	Basaltic trachy-andesite
SiO_2 (wt. %)	50.80	50.50	50.60	50.70	50.50	50.80
TiO_2	2.13	2.15	2.14	2.10	2.13	2.14
Al_2O_3	16.30	16.30	16.40	16.50	16.40	16.20
$Fe_2O_{3\ Tot}$	9.28	9.57	9.43	9.31	9.52	9.49
MnO	0.15	0.16	0.16	0.16	0.16	0.15
MgO	3.93	4.02	4.13	4.00	4.11	4.04
CaO	7.52	7.62	7.48	7.46	7.45	7.42
Na_2O	5.69	5.59	5.45	5.64	5.57	5.63
K_2O	2.65	2.58	2.51	2.55	2.57	2.55
P_2O_5	1.09	1.08	1.07	1.07	1.06	1.07
LOI	0.35	0.36	0.56	0.43	0.45	0.40
Total	99.89	99.93	99.93	99.92	99.92	99.89
mg#	48.65	48.45	49.51	49.05	49.15	48.79
Ni (ppm)	45.6	44.7	46.6	46.8	47.3	44.9
Co	24.1	24.1	25.5	26.2	25.0	27.1
Cr	195	182	210	173	174	164
V	157	157	161	155	158	158
Sc	19.6	19.9	20.5	18.6	20.8	18.6
Sr	682	689	681	674	685	678
Rb	32.4	32.2	31.2	31.3	32.1	32.3
Ba	398	393	376	390	387	387
Zr	256	256	253	251	254	252
Nb	49.5	49.4	49.6	47.2	49.8	48.2
Th	4.63	4.24	5.22	4.66	5.75	3.15
Y	20.4	21.3	20.5	20.6	21.4	20.5
La	26.9	26.9	29.0	29.3	25.8	25.5
Ce	91.8	91.7	96.6	98.1	88.4	78.6
Nd	37.8	38.5	36.3	37.9	36.5	38.2
Pb	9.44	9.60	6.58	10.8	12.0	12.3
Zn	66.4	70.2	67.3	66.3	66.6	67.5
Cu	39.7	38.3	40.0	38.9	38.9	40.4
Ga	30.3	35.2	28.6	27.5	28.0	27.7

Mg# ((MgO/(MgO+FeO) mol %) is calculated with Fe_2O_3=0.15*FeO (*Green et al., 1974*)

Table 2: Representative major element composition (in wt. %) of olivines of Estancia Sol de Mayo (ESM) mantle xenoliths.

Sample	MGP2b		MGP2b2		MGP1b		MGP1g		MGP3b		MGP4b		MGP1h		MGP2a		MGP1d	
phase	ol rim	ol core	ol rim	ol core	ol rim	ol core	ol rim	ol core	ol rim	ol core	ol rim	ol core	ol rim	ol core	ol rim	ol core	ol rim	ol core
Host rock	Lherzolite		Lherzolite		Harzburgite		Harzburgite		Harzburgite		Harzburgite		Dunite		Dunite		Wehrlite	
SiO_2	40.60	41.36	41.30	41.32	40.39	40.01	40.05	39.22	40.83	40.89	41.00	41.25	40.73	40.44	39.87	39.63	39.35	38.86
FeO	8.74	9.11	8.83	9.08	11.25	11.60	14.14	15.01	10.60	9.74	8.13	8.20	9.03	8.96	9.76	10.32	16.96	17.40
MnO	0.21	0.25	0.15	0.17	0.22	0.17	0.16	0.20	0.20	0.12	0.12	0.15	0.10	0.12	0.14	0.24	0.25	0.20
MgO	50.26	50.20	49.34	49.86	47.68	48.08	46.15	45.43	49.13	49.36	50.87	50.39	49.14	49.07	48.94	49.20	43.66	43.62
CaO	0.07	0.04	0.01	0.06	0.09	0.09	0.13	0.04	0.08	0.04	<0.01	0.15	0.07	<0.01	0.08	0.05	0.07	0.07
NiO	0.50	0.27	0.46	0.36	0.34	0.46	0.25	0.23	0.35	<0.01	0.41	<0.01	0.34	0.37	0.21	0.45	0.15	0.23
Cr_2O_3	<0.01	0.09	0.02	0.01	0.12	0.11	0.06	<0.01	0.07	0.08	0.13	0.18	0.02	<0.01	<0.01	0.03	0.02	0.02
Total	100.38	101.32	100.11	100.86	100.09	100.52	100.94	100.13	101.26	100.23	100.66	100.32	99.43	98.96	99.00	99.92	100.46	100.40
Fo	91.11	90.76	90.88	90.73	88.31	88.08	85.33	84.36	89.20	90.03	91.77	91.63	90.65	90.71	89.94	89.47	82.10	81.71
Si	1.003	1.022	1.020	1.021	0.998	0.988	0.989	0.969	1.009	1.010	1.013	1.019	1.006	0.999	0.985	0.979	0.972	0.960
Fe^{2+}	0.181	0.188	0.182	0.188	0.232	0.240	0.292	0.310	0.219	0.201	0.168	0.169	0.187	0.185	0.202	0.213	0.350	0.359
Mn	0.004	0.005	0.003	0.004	0.005	0.004	0.003	0.004	0.004	0.003	0.003	0.003	0.002	0.003	0.003	0.005	0.005	0.004
Mg	1.851	1.849	1.817	1.836	1.756	1.770	1.699	1.673	1.809	1.818	1.873	1.856	1.809	1.807	1.802	1.812	1.608	1.606
Ca	0.002	0.001	0.000	0.002	0.002	0.002	0.003	0.001	0.002	0.001	0.000	0.004	0.002	0.000	0.002	0.001	0.002	0.002
Ni	0.010	0.005	0.009	0.007	0.007	0.009	0.005	0.005	0.007	0.000	0.008	0.000	0.007	0.007	0.004	0.009	0.003	0.005
Cr	0.000	0.001	0.000	0.000	0.001	0.001	0.001	0.000	0.001	0.001	0.001	0.002	0.000	0.000	0.000	0.000	0.000	0.000
Sum cat	3.050	3.071	3.032	3.057	3.001	3.015	2.993	2.962	3.051	3.033	3.066	3.054	3.013	3.001	2.999	3.020	2.941	2.937

Ol: olivine; Fo: forsterite.

Table 3: Representative major element composition (in wt. %) of clinopyroxenes of Estancia Sol de Mayo (ESM).

Sample	MGP2b		MGP2b2		MGP1b		MGP1c		MGP3b		MGP4b		MGP1h		MGP2a		MGP1d	
phase	cpx 1 core	cpx 2 rim	cpx 1 rim	cpx 2 core	cpx 1 core	cpx 2 core	cpx 2 core	cpx 2 core	cpx 1 rim	cpx 1 core	cpx 1 core	cpx 2 core	cpx 2 core	cpx 2 rim	cpx 1 core	cpx 2 core	cpx 1 core	cpx 2 core
Host rock	Lherzolite		Lherzolite		Harzburgite		Harzburgite		Harzburgite		Harzburgite		Dunite		Dunite		Wehrlite	
SiO_2	52.43	52.33	51.93	52.78	52.90	52.15	52.45	52.25	53.47	53.48	53.05	52.62	51.83	52.77	53.27	52.85	49.91	49.44
TiO_2	0.17	0.19	0.16	0.28	0.13	0.17	0.28	0.31	0.10	0.11	0.25	0.25	0.24	0.24	0.07	0.30	1.01	1.17
Al_2O_3	4.06	3.96	3.22	4.04	3.10	3.56	3.46	4.13	2.34	2.69	4.00	4.20	3.78	3.76	1.93	2.65	6.50	7.30
Cr_2O_3	1.03	1.45	1.20	1.21	0.92	0.96	1.32	1.38	1.06	1.45	1.28	1.36	1.25	1.33	0.87	1.04	0.60	0.71
FeO	2.91	2.9	2.94	2.99	3.75	3.69	3.07	3.07	3.03	2.98	2.75	2.80	3.13	3.20	3.05	3.16	4.98	5.07
MnO	0.15	<0.01	0.15	0.11	0.16	0.16	0.10	0.07	0.09	0.03	0.10	0.05	0.10	0.06	0.09	0.14	0.15	0.20
MgO	16.68	16.60	17.16	16.80	16.82	16.70	16.49	16.34	17.24	17.01	16.99	17.14	16.49	16.55	17.45	17.11	14.69	14.55
CaO	20.95	21.59	21.24	21.05	21.12	20.98	21.29	21.05	21.32	21.04	21.15	21.02	20.76	21.07	21.21	20.49	20.57	20.60
Na_2O	0.81	0.99	0.81	0.91	0.81	0.78	1.05	0.95	0.92	0.92	1.09	1.03	1.04	1.06	0.95	1.18	0.96	1.00
Total	99.19	99.97	98.81	100.17	99.71	99.15	99.51	99.55	99.57	99.71	100.66	100.47	98.62	100.04	98.89	98.92	99.37	100.04
mg#	91.1	91.2	91.2	90.9	88.9	89.0	90.5	90.5	91.0	91.1	91.7	91.6	90.4	90.2	91.1	90.6	84.0	83.6
Si	1.913	1.895	1.901	1.907	1.925	1.907	1.910	1.903	1.943	1.944	1.904	1.891	1.902	1.910	1.946	1.930	1.833	1.804
Ti	0.005	0.005	0.004	0.008	0.004	0.005	0.008	0.008	0.003	0.003	0.007	0.007	0.007	0.007	0.002	0.008	0.028	0.032
Al	0.175	0.169	0.139	0.172	0.133	0.153	0.148	0.177	0.100	0.115	0.169	0.178	0.164	0.160	0.083	0.114	0.281	0.314
Fe^{3+}	0.004	0.015	0.019	0.007	0.010	0.013	0.013	0.007	0.011	0.004	0.012	0.015	0.014	0.011	0.016	0.016	0.012	0.017
Fe^{2+}	0.085	0.072	0.071	0.083	0.104	0.100	0.081	0.087	0.081	0.087	0.070	0.069	0.082	0.086	0.077	0.081	0.141	0.138
Mn	0.005	0.000	0.005	0.003	0.005	0.005	0.003	0.002	0.003	0.001	0.003	0.002	0.003	0.002	0.003	0.004	0.005	0.006
Mg	0.907	0.896	0.936	0.905	0.912	0.910	0.895	0.887	0.934	0.921	0.909	0.918	0.902	0.893	0.950	0.931	0.804	0.791
Ca	0.819	0.838	0.833	0.815	0.823	0.822	0.830	0.822	0.830	0.819	0.813	0.810	0.816	0.817	0.830	0.802	0.810	0.805
Na	0.057	0.070	0.057	0.064	0.057	0.055	0.074	0.067	0.065	0.065	0.076	0.072	0.074	0.074	0.067	0.084	0.068	0.071
Cr	0.030	0.042	0.035	0.035	0.026	0.028	0.038	0.040	0.030	0.042	0.036	0.039	0.036	0.038	0.025	0.030	0.017	0.020
Sum cat	4.000	4.002	4.000	3.999	3.999	3.998	4.000	4.000	4.000	4.001	3.999	4.001	4.000	3.998	3.999	4.000	3.999	3.998

All Fe as Fe^{+2}; mg# = 100 x [Mg/(Mg + Fe)]; Fe^{+2} and Fe^{+3} calculated by stoichiometry of the formula unit.

Table 4: Representative major element composition (in wt. %) of orthopyroxenes of Estancia Sol de Mayo (ESM).

Sample	MGP2b		MGP2b2		MGP1b		MGP1c		MGP1g		MGP3b		MGP4b		MGP2a		
phase	opx1 rim	opx2 core	opx1 rim	opx2 core	opx1 core	opx2 core	opx1 core	opx2 rim	opx1 core	opx2 core	opx1 rim	opx2 core	opx1 rim	opx2 core	opx3	opx3	opx3
Host rock	Lherzolite		Lherzolite		Harzburgite		Harzburgite		Harzburgite		Harzburgite		Harzburgite		Dunite		
SiO_2	55.61	56.33	56.12	55.24	55.79	55.55	56.75	56.22	54.43	54.87	56.78	56.67	56.25	56.30	55.10	55.00	55.17
TiO_2	0.03	0.08	0.06	0.02	<0.01	0.04	<0.01	0.08	0.21	0.11	0.05	0.02	0.08	0.06	0.04	0.01	0.06
Al_2O_3	2.75	2.67	2.84	2.76	2.30	2.61	1.39	1.83	3.10	2.98	1.69	1.57	2.77	2.67	3.37	3.27	3.15
FeOtot	5.82	5.81	5.65	6.02	7.97	7.62	5.67	6.31	9.31	9.05	5.90	6.01	5.16	5.33	6.48	6.21	6.26
MnO	0.14	0.17	0.24	0.16	0.07	0.19	0.24	0.15	0.17	0.26	0.17	0.16	0.14	0.09	0.16	0.14	0.09
MgO	33.89	33.91	33.86	33.92	33.05	32.84	34.79	34.30	31.50	31.69	34.14	34.31	34.58	34.62	33.31	33.39	33.53
CaO	0.94	0.97	0.89	0.99	0.96	0.90	0.72	0.91	0.87	0.94	0.94	0.96	0.87	0.86	0.83	0.85	0.76
Na_2O	<0.01	<0.01	<0.01	<0.01	<0.01	<0.01	<0.01	<0.01	<0.01	<0.01	<0.01	<0.01	<0.01	<0.01	<0.01	<0.01	<0.01
Cr_2O_3	0.70	0.52	0.51	0.57	0.58	0.54	0.26	0.51	0.38	0.42	0.53	0.56	0.70	0.56	0.33	0.22	0.24
Tot	99.88	100.46	100.17	99.68	100.72	100.29	99.82	100.31	99.97	100.32	100.20	100.26	100.55	100.49	99.62	99.09	99.26
mg#	91.2	91.2	91.4	90.9	88.1	88.5	91.6	90.6	85.8	86.2	91.2	91.1	92.3	92.1	90.2	90.6	90.5
Si	1.919	1.934	1.931	1.908	1.924	1.923	1.950	1.932	1.904	1.912	1.955	1.949	1.922	1.925	1.908	1.913	1.915
Ti	0.001	0.002	0.002	0.001	0.000	0.001	0.000	0.002	0.006	0.003	0.001	0.001	0.002	0.002	0.001	0.000	0.002
Al	0.112	0.108	0.115	0.112	0.094	0.107	0.056	0.074	0.128	0.122	0.069	0.064	0.112	0.108	0.138	0.134	0.129
Fe^{3+}	0.007	0.002	0.002	0.014	0.010	0.007	0.009	0.011	0.011	0.009	0.001	0.005	0.005	0.006	0.009	0.008	0.008
Fe^{2+}	0.160	0.165	0.161	0.160	0.219	0.213	0.163	0.170	0.261	0.254	0.169	0.167	0.142	0.146	0.179	0.172	0.174
Mn	0.004	0.005	0.007	0.005	0.002	0.006	0.007	0.004	0.005	0.008	0.005	0.005	0.004	0.003	0.005	0.004	0.003
Mg	1.743	1.735	1.736	1.746	1.699	1.695	1.781	1.757	1.642	1.645	1.751	1.759	1.761	1.764	1.719	1.731	1.734
Ca	0.035	0.036	0.033	0.037	0.035	0.033	0.026	0.034	0.033	0.035	0.035	0.035	0.032	0.032	0.031	0.032	0.028
Na	0.000	0.000	0.000	0.000	0.000	0.000	0.000	0.000	0.000	0.000	0.000	0.000	0.000	0.000	0.000	0.000	0.000
Cr	0.019	0.014	0.014	0.016	0.016	0.015	0.007	0.014	0.010	0.012	0.014	0.015	0.019	0.015	0.009	0.006	0.007
Sum cat	4.000	4.001	4.001	3.999	3.999	4.000	3.999	3.998	4.000	4.000	4.000	4.000	3.999	4.001	3.999	4.000	4.000

All Fe as Fe^{+2}; mg# = 100 x [Mg/(Mg + Fe)]; Fe^{+2} and Fe^{+3} calculated by stoichiometry of the formula unit.

Table 5: Representative major element composition (in wt. %) of spinels of Estancia Sol de Mayo (ESM).

Sample	MGP2b		MGP2b2		MGP1b		MGP1c		MGP1g		MGP3b		MGP4b		MGP1h		MGP2a		MGP1d	
phase	sp_{cpx} rim	sp_{cpx} core	sp_{cpx} core	sp_{cpx} rim	sp_{cpx} core	sp core	sp_{cpx} core	sp core	sp core	sp rim	sp core	sp rim	sp_{cpx} core	sp_{cpx} rim	sp_{cpx} core	sp rim	sp_{cpx} core	sp core	sp_{cpx} rim	sp core
Host rock	Lherzolite		Lherzolite		Harzburgite		Harzburgite		Harzburgite		Harzburgite		Harzburgite		Dunite		Dunite		Wehrlite	
SiO_2	0.04	0.06	0.04	0.01	0.09	0.10	0.07	<0.01	0.09	0.11	0.09	0.06	0.03	0.07	0.03	0.04	0.03	0.03	0.02	<0.01
TiO_2	0.27	0.43	0.24	0.19	0.29	0.28	0.43	0.42	1.70	2.05	0.42	0.35	0.20	0.13	0.36	0.39	0.73	0.53	0.49	0.38
Al_2O_3	34.91	35.86	35.36	34.89	28.72	28.88	27.32	26.29	34.90	35.02	19.96	19.71	33.45	33.72	29.25	22.83	25.06	21.59	45.40	48.00
Cr_2O_3	32.69	31.46	32.20	32.07	31.80	32.24	36.67	37.96	18.75	18.27	43.93	43.88	33.89	33.08	34.09	41.43	38.81	42.20	17.79	15.20
Fe_2O_3	2.20	2.62	3.24	3.69	9.48	9.61	6.50	6.69	13.15	12.24	7.46	7.39	3.63	3.73	6.58	7.33	5.12	6.40	4.26	4.65
FeO	11.68	11.43	11.55	11.10	15.18	15.09	13.00	13.36	17.59	19.09	13.59	13.81	10.40	9.96	12.18	13.35	13.95	14.37	16.01	15.28
MnO	0.23	0.22	0.24	0.19	0.18	0.21	0.26	0.14	0.23	0.16	0.22	0.15	0.10	0.19	0.14	0.27	0.16	0.20	0.17	0.10
MgO	16.67	17.04	16.90	16.95	13.83	14.09	15.14	14.87	13.80	13.07	14.15	13.79	17.35	17.50	15.61	14.56	14.27	13.68	15.06	15.83
NiO	<0.01	0.23	0.22	0.29	0.28	0.26	0.21	0.25	0.24	0.24	0.14	0.20	0.25	0.15	0.28	0.21	0.16	0.12	0.24	0.21
Tot	98.69	99.35	99.99	99.38	99.85	100.76	99.60	99.98	100.45	100.25	99.96	99.34	99.30	98.53	98.52	100.41	98.29	99.12	99.44	99.65
mg#	71.8	72.7	72.3	73.1	61.9	62.5	67.5	66.5	58.3	55.0	65.0	64.0	74.8	75.8	69.5	66.0	64.6	62.9	62.6	64.9
cr#	38.6	37.1	37.9	38.1	42.6	42.8	47.4	49.2	26.5	25.9	59.6	59.9	40.5	39.7	43.9	54.9	51.0	56.7	20.8	17.5
Si	0.001	0.002	0.001	0.000	0.003	0.003	0.002	0.000	0.003	0.003	0.003	0.002	0.001	0.002	0.001	0.001	0.001	0.001	0.001	0.000
Ti	0.006	0.009	0.005	0.004	0.007	0.006	0.010	0.009	0.037	0.045	0.010	0.008	0.004	0.003	0.008	0.009	0.017	0.012	0.010	0.008
Al	1.190	1.210	1.191	1.182	1.014	1.010	0.963	0.930	1.199	1.210	0.727	0.725	1.138	1.151	1.030	0.817	0.906	0.789	1.496	1.557
Fe^{3+}	0.050	0.060	0.070	0.080	0.210	0.210	0.150	0.150	0.290	0.270	0.170	0.170	0.080	0.080	0.150	0.170	0.120	0.150	0.090	0.100
Fe^{2+}	0.280	0.270	0.280	0.270	0.380	0.370	0.330	0.340	0.430	0.470	0.350	0.360	0.250	0.240	0.300	0.340	0.360	0.370	0.370	0.350
Mn	0.006	0.005	0.006	0.005	0.005	0.005	0.007	0.004	0.006	0.004	0.006	0.004	0.002	0.005	0.004	0.007	0.004	0.005	0.004	0.002
Mg	0.719	0.727	0.719	0.726	0.618	0.623	0.675	0.665	0.600	0.571	0.652	0.641	0.746	0.755	0.695	0.659	0.652	0.632	0.627	0.649
Cr	0.748	0.712	0.727	0.729	0.753	0.756	0.867	0.900	0.432	0.423	1.074	1.082	0.773	0.758	0.805	0.995	0.941	1.035	0.393	0.331
Ni	0.000	0.005	0.005	0.007	0.007	0.006	0.005	0.006	0.006	0.006	0.003	0.005	0.006	0.003	0.007	0.005	0.004	0.003	0.005	0.005
Sum cat	3.000	3.000	3.004	3.003	2.997	2.989	3.009	3.004	3.003	3.002	2.995	2.997	3.000	2.997	3.000	3.003	3.005	2.997	2.996	3.002

Mg# = 100 x [Mg/(Mg + Fe)]; cr# = 100 x [Cr/(Cr + Al)]; Fe^{+2} and Fe^{+3} calculated by stoichiometry of the formula unit.

Table 6: Trace element contents (ppm) of Estancia Sol de Mayo (ESM) clinopyroxenes.

Sample	MGP2b				MGP2b2														
phase	cpx2	cpx2	cpx2	cpx2	cpx1	cpx1	cpx1	cpx1	cpx1	cpx1	cpx1	cpx1	cpx2	cpx2	cpx2	cpx2	cpx2	cpx2	cpx2
Rock type	Lherzolite				Lherzolite														
Ba	5.40	n.d.	n.d.	1.57	0.65	1.39	0.33	n.d.	1.42	0.40	1.21	n.d.	n.d.	n.d.	n.d.	n.d.	1.74	n.d.	0.10
Th	14.2	n.d.	10.4	n.d.	3.29	2.75	2.35	n.d.	3.06	2.35	2.00	n.d.	n.d.	2.12	n.d.	n.d.	6.26	0.24	4.24
Nb	1.21	1.58	0	1.11	1.15	0.80	0.7	0.63	0.76	0.66	0.55	0.52	0.70	0.93	0.70	0.90	0.94	0.53	0.67
La	3.84	4.69	4.14	4.25	3.77	3.70	3.42	3.74	4.28	3.64	3.61	3.95	3.69	3.02	4.24	n.d.	n.d.	5.41	9.38
Ce	9.10	11.3	10.5	10.8	9.86	9.89	9.10	9.56	8.45	9.81	8.01	9.17	8.22	8.58	n.d.	n.d.	n.d.	14.1	26.7
Sr	97.4	n.d.	n.d.	n.d.	96.9	102	98.3	102	101	98.6	90.1	102	95.7	92.8	124	123	108	128	201
Nd	5.66	7.43	6.35	5.95	4.93	5.89	4.95	5.37	4.45	6.21	n.d.	5.84	4.38	n.d.	9.05	9.32	n.d.	8.20	14.8
Zr	21.3	21.5	19.6	18.0	21.7	20.7	18.4	16.4	19.1	17.1	8.79	12.6	19.4	19	31.4	28.6	27.0	19.4	74.2
Sm	1.49	2.34	2.12	2.28	1.54	1.82	1.25	0.66	1.31	1.57	n.d.	0.92	1.73	0.93	3.08	n.d.	2.22	1.84	3.31
Eu	0.45	0.41	0.64	0.74	0.37	0.57	0.59	0.32	0.46	0.32	0.51	0.21	0.38	0.28	n.d.	n.d.	0.87	0.51	n.d.
Ti	1694	1565	1452	1432	1726	1502	1330	1276	1479	1275	1105	1092	1455	1479	1290	1295	1285	1119	2622
Gd	1.60	n.d.	1.67	n.d.	1.19	1.60	0.72	1.48	n.d.	n.d.	1.60	n.d.	1.34	n.d.	1.66	2.88	2.85	n.d.	n.d.
Dy	1.99	1.43	1.70	0.99	1.62	1.92	1.40	1.80	1.97	1.81	1.71	n.d.	1.24	n.d.	2.13	2.39	2.56	n.d.	2.30
Er	1.40	0.79	1.36	0.78	1.04	n.d.	0.83	0.39	1.44	1.24	n.d.	0.98	1.32	0.79	1.03	1.46	1.52	1.17	1.11
Yb	1.54	1.01	1.42	n.d.	n.d.	1.25	1.25	0.71	n.d.	0.95	n.d.	0.62	1.20	1.40	1.03	1.62	1.39	1.05	1.33
Lu	0.26	0.18	n.d.	n.d.	n.d.	0.18	0.17	n.d.	n.d.	n.d.	0.14	n.d.	0.22	n.d.	n.d.	0.23	0.27	0.13	n.d.

n.d.: not detected.

Table 6 continued

Sample						MGP1b				MGP1c		MGP3b					MGP4b				
phase	cpx2	cpx2	cpx2	cpx2	cpx2	cpx2	cpx2	cpx2	cpx2	cpx2	cpx2	cpx1	cpx1	cpx1	cpx1	cpx1	cpx1	cpx1	cpx1	cpx1	cpx1
Rock type						Harzburgite				Harzburgite		Harzburgite					Harzburgite				
Ba	0.65	n.d.	0.04	1.88	n.d.	1.17	4.13	n.d.	n.d.	n.d.	n.d.	1.95	1.24	0.56	0.57	n.d.	n.d.	n.d.	n.d.	n.d.	0.66
Th	1.29	10.7	n.d.	n.d.	n.d.	8.12	n.d.	4.82	8.59	4.71	8.24	2.35	4.00	2.35	1.29	n.d.	3.76	14.2	1.29	n.d.	2.35
Nb	0.91	n.d.	0.93	0.65	0.46	0.69	0.07	0.39	0.17	1.22	1.09	0.42	0.42	0.04	0.25	0.31	0.89	1.16	0.66	0.46	1.28
La	4.13	4.58	3.79	4.45	n.d.	5.98	5.78	5.55	4.84	7.30	7.87	5.56	6.80	6.26	6.45	6.66	n.d.	7.54	4.67	6.61	5.10
Ce	13.4	n.d.	9.86	n.d.	13.0	n.d.	14.8	12.6	13.2	21.3	25.3	13.8	n.d.	16.8	17.3	n.d.	n.d.	24.8	n.d.	n.d.	12.7
Sr	120	113	103	130	114	n.d.	n.d.	106	99.6	176	162	160	190	181	177	200	135	199	132	n.d.	112
Nd	9.82	8.34	5.73	9.72	8.48	9.87	7.29	8.13	5.77	14.4	21.0	n.d.	9.85	8.01	8.03	11.5	n.d.	16.5	10.2	9.69	8.71
Zr	30.4	28.9	21.5	33.5	25.9	6.19	5.14	5.75	6.89	55.0	65.6	11.5	17.8	15.3	16.6	21.0	32.9	62.1	32.0	7.42	6.24
Sm	3.33	n.d.	1.65	2.92	2.40	n.d.	2.48	n.d.	1.41	4.64	4.11	2.04	2.37	1.42	2.61	n.d.	3.76	4.65	2.19	n.d.	2.53
Eu	0.80	n.d.	0.31	n.d.	n.d.	n.d.	0.49	0.81	0.64	1.51	1.11	0.39	0.50	n.d.	0.66	n.d.	n.d.	1.28	0.75	0.80	0.66
Ti	1318	1414	1558	1234	1197	923	890	1003	958	1463	n.d.	631	861	725	753	933	1345	1512	1285	897	875
Gd	n.d.	n.d.	1.72	2.19	n.d.	1.82	1.97	3.23	2.67	4.52	n.d.	1.37	1.42	n.d.	1.12	n.d.	3.36	3.84	2.53	n.d.	n.d.
Dy	2.70	n.d.	2.12	2.09	2.99	3.17	2.73	n.d.	3.72	n.d.	n.d.	1.60	1.35	1.93	1.18	2.04	2.84	3.68	2.60	n.d.	1.25
Er	n.d.	n.d.	1.38	1.12	1.15	n.d.	n.d.	n.d.	2.70	2.28	n.d.	0.80	0.82	n.d.	n.d.	0.92	1.38	1.95	1.11	2.07	n.d.
Yb	n.d.	1.15	1.25	1.08	n.d.	2.84	1.94	2.37	n.d.	2.51	1.93	n.d.	0.67	1.00	n.d.	0.99	1.38	2.12	n.d.	n.d.	1.40
Lu	n.d.	n.d.	0.18	n.d.	n.d.	n.d.	n.d.	n.d.	n.d.	0.38	0.22	n.d.	n.d.	n.d.	n.d.	n.d.	0.27	0.47	n.d.	n.d.	n.d.

Table 6 continued

Sample						MGP2a	MGP1d													
phase	cpx1	cpx2	cpx2	cpx2	cpx2	cpx1	cpx1	cpx1	cpx1	cpx1	cpx1	cpx1	cpx1	cpx1	cpx1	cpx1	cpx1	cpx1	cpx1	cpx1
Rock type						Dunite	Wehrlite													
Ba	0.71	1.48	5.10	2.17	4.13	n.d.	6.42	n.d.	7.94	n.d.	n.d.	0.82	5.53	1.56	3.05	5.52	1.65	3.40	0.21	n.d.
Th	0.71	1.41	n.d.	n.d.	2.59	2.00	n.d.	10.0	n.d.	5.06	n.d.	6.94	13.9	n.d.	3.53	15.8	n.d.	n.d.	8.12	n.d.
Nb	1.29	0.72	0.42	0.11	0.45	0.22	1.33	0.13	0.81	0.74	0.74	0.66	0.42	0.69	1.33	0.36	0.83	0.73	0.70	1.00
La	5.69	4.43	5.94	6.12	4.10	6.07	3.40	2.97	2.09	1.90	3.13	4.77	3.23	5.60	3.83	3.65	3.80	3.73	3.93	2.04
Ce	15.3	10.6	14.6	n.d.	8.36	16.7	9.71	8.52	9.33	n.d.	10.1	10.3	10.5	11.2	9.77	12.36	9.15	9.03	10.0	8.25
Sr	n.d.	101	n.d.	n.d.	94.8	136	n.d.	68.5	64.6	64.4	n.d.	n.d.	n.d.	98.5	99.1	61.6	92.5	98.1	n.d.	68.2
Nd	8.96	5.91	8.16	8.55	5.38	9.68	9.70	8.14	10.1	n.d.	8.48	6.49	9.12	7.37	7.27	n.d.	5.81	4.45	5.40	8.08
Zr	5.79	3.95	5.85	6.79	4.96	17.6	34.0	35.8	29.6	27.7	37.6	17.6	52.6	20.7	14.6	54.9	17.8	12.3	16.3	31.4
Sm	n.d.	1.78	n.d.	n.d.	n.d.	2.70	2.62	4.44	n.d.	n.d.	n.d.	1.41	n.d.	2.17	1.52	3.76	1.91	n.d.	1.70	n.d.
Eu	0.38	0.66	n.d.	0.98	n.d.	0.84	n.d.	1.47	n.d.	n.d.	n.d.	n.d.	n.d.	0.73	n.d.	1.04	0.69	0.49	0.41	1.25
Ti	807	759	913	799	770	803	5326	6158	5476	4957	6005	1391	6860	1343	1112	7710	1203	1073	1231	5373
Gd	1.56	2.32	2.26	n.d.	n.d.	1.62	n.d.	4.50	6.28	2.74	5.39	n.d.	n.d.	n.d.	n.d.	n.d.	n.d.	n.d.	1.44	3.60
Dy	2.20	3.65	n.d.	n.d.	1.73	1.34	3.31	5.28	4.14	3.13	n.d.	n.d.	n.d.	2.86	n.d.	5.88	2.36	n.d.	1.82	3.42
Er	n.d.	2.88	n.d.	n.d.	1.57	0.95	n.d.	3.25	2.64	n.d.	n.d.	0.72	3.62	2.04	1.59	n.d.	1.61	1.94	1.14	1.09
Yb	n.d.	n.d.	n.d.	2.61	3.37	1.06	n.d.	n.d.	2.66	1.14	1.90	n.d.	1.64	n.d.	n.d.	1.67	1.72	n.d.	1.13	0.82
Lu	n.d.	n.d.	n.d.	n.d.	n.d.	n.d.	n.d.	0.20	n.d.	n.d.	n.d.	n.d.	n.d.	n.d.	n.d.	n.d.	n.d.	n.d.	n.d.	n.d.

Table 7: Trace element contents (ppm) of Estancia Sol de Mayo (ESM) orthopyroxenes.

Sample	MGP2b		MGP2b2		MGP1b			MGP1c		MGP1g				MGP3b		MGP4b		MGP1h		MGP2a		
phase	opx1	opx1	opx1	opx1	opx1	opx2	opx2	opx1	opx2	opx1	opx1	opx2	opx2	opx1	opx2	opx1	opx1	opx1	opx2	opx3	opx3	opx3
Rock type	Lherzolite		Lherzolite		Harzburgite			Harzburgite		Harzburgite				Harzburgite		Harzburgite		Dunite		Dunite		
Ba	0.28	0.65	0.61	0.38	0.61	n.d.	n.d.	0.94	0.72	n.d.	0.53	0.65	0.72	0.72	0.80	0.69	0.69	0.62	n.d.	n.d.	n.d.	0.46
Th	0.19	0.12	0.13	n.d.	0.13	0.17	0.20	0.11	0.11	0.10	0.19	n.d.	n.d.	0.16	0.16	n.d.	n.d.	0.13	n.d.	n.d.	n.d.	0.16
Nb	0.45	0.11	0.45	n.d.	0.27	0.45	n.d.	0.32	0.31	n.d.	0.46	n.d.	0.10	0.44	0.35	0.15	0.40	0.34	0.42	0.12	n.d.	0.36
La	0.12	0.06	0.35	n.d.	0.19	0.21	0.17	0.14	0.18	0.14	0.18	n.d.	0.18	0.16	0.35	0.27	0.40	n.d.	0.15	0.25	0.21	0.34
Ce	0.15	0.22	0.35	0.28	0.23	0.25	0.33	0.12	0.24	0.45	0.47	0.55	0.48	0.37	0.45	0.27	0.38	0.28	0.35	0.75	0.61	0.50
Sr	0.19	0.59	0.17	0.33	0.46	0.19	0.54	0.61	0.66	0.36	0.52	0.57	0.53	0.32	0.46	0.65	0.36	0.58	0.29	1.26	0.96	0.81
Nd	n.d.	0.62	1.35	1.25	0.45	0.61	n.d.	n.d.	1.26	0.70	0.72	0.80	0.69	0.40	0.61	n.d.	0.35	0.46	0.39	0.75	0.70	0.59
Zr	1.30	0.93	1.13	0.94	1.28	0.97	1.12	2.01	2.26	5.54	4.74	5.04	4.67	1.02	1.33	1.52	2.43	1.27	2.64	21.4	17.5	20.0
Sm	0.32	0.35	0.63	0.59	0.31	0.45	0.40	0.61	0.68	0.35	0.34	0.40	0.33	0.21	0.32	0.17	0.18	0.28	0.22	0.42	0.41	0.37
Eu	0.19	0.18	0.29	0.25	0.23	n.d.	n.d.	0.29	n.d.	0.17	n.d.	0.21	0.18	0.11	0.16	n.d.	0.12	n.d.	0.12	0.23	n.d.	0.21
Ti	408	508	490	519	357	300	294	248	358	1306	1286	1081	743	331	377	314	435	254	217	635	362	400
Gd	0.81	0.82	n.d.	1.00	1.09	1.05	1.27	1.21	1.25	0.65	0.75	0.86	0.79	0.50	0.73	0.40	0.47	0.53	0.45	n.d.	0.78	0.81
Dy	1.06	1.09	1.31	1.07	1.37	1.32	1.51	1.23	1.28	0.85	1.00	1.20	1.08	0.56	0.77	0.49	0.60	0.67	0.58	1.10	1.00	1.02
Er	0.69	0.71	0.84	0.69	0.89	0.86	n.d.	0.75	0.74	0.60	0.71	0.81	0.78	0.36	0.53	0.33	0.39	0.41	0.36	0.69	0.68	0.67
Yb	0.70	0.72	0.82	0.73	0.90	0.88	n.d.	0.74	0.72	0.61	0.72	0.81	0.77	0.35	0.52	0.33	0.39	0.39	0.36	0.70	0.69	0.68
Lu	n.d.	n.d.	0.12	0.10	0.14	0.13	0.14	0.12	0.12	n.d.	0.11	n.d.	0.12	0.06	0.08	0.05	0.06	n.d.	0.06	n.d.	0.10	0.11

n.d.: not detected.

Table 8: Equilibration temperature, pressure and fO_2 estimates of Estancia Sol de Mayo (ESM) mantle xenoliths.

Sample	Lhitology	Area	Cpx	Opx	Ol	T°C+	mean T°C	T°C*	P Kbar	Δ log fO_2
MGP2b	Lherzolite	Area 2	7	6	4	1055			*33*	
		Area 6	3	5	8	1011			20	
		Area 8	6	11	8	1026	**1031**	**945**	*38*	**0.02**
MGP2b2	Lherzolite	Area 2	8	9	5	1026			16	
		Area 1	3	4	8	1041			18	
		Area 7	10	5	5	943	**1003**	**913**	*3*	**0.62**
MGP1b	Harzburgite	Area 2	2	1	3	1041			24	
		Area 3	1	2	3	1008			*2*	
		Area 5	2	1	4	995			*-5*	
		Area 6	4	3	3	992			*-2*	
		Area 7	3	2	5	1002			*1*	
		Area 8	3	4	6	1017	**1009**	**912**	*3*	**1.26**
MGP3b	Harzburgite	Area 4	2	3	9	1012			15	
		Area 4	8	6	9	1017			16	
		Area 5	2	4	5	1003			5	
		Area 7	2	8	3	1028	**1015**	**954**	12	**1.47**
MGP4b	Harzburgite	Area 3	1	6	1	1044			13	
		Area 4	7	9	2	1027			11	
		Area 5	1	6	6	1037			*2*	
		Area 7	10	14	8	1040			13	
		Area 7	3	6	15	1053	**1040**	**980**	*-10*	**1.01**

T °C+ calculated after *Brey and K ö hler (1990)*
T °C* calculated after *Ballhaus et al. (1991)*
P Kbar calculated after *Köhler and Brey (1990)*
ΔlogfO_2 calculated usind T after *Brey and Köhler (1990)*
italics unreasonably low and/or high and negative pressures

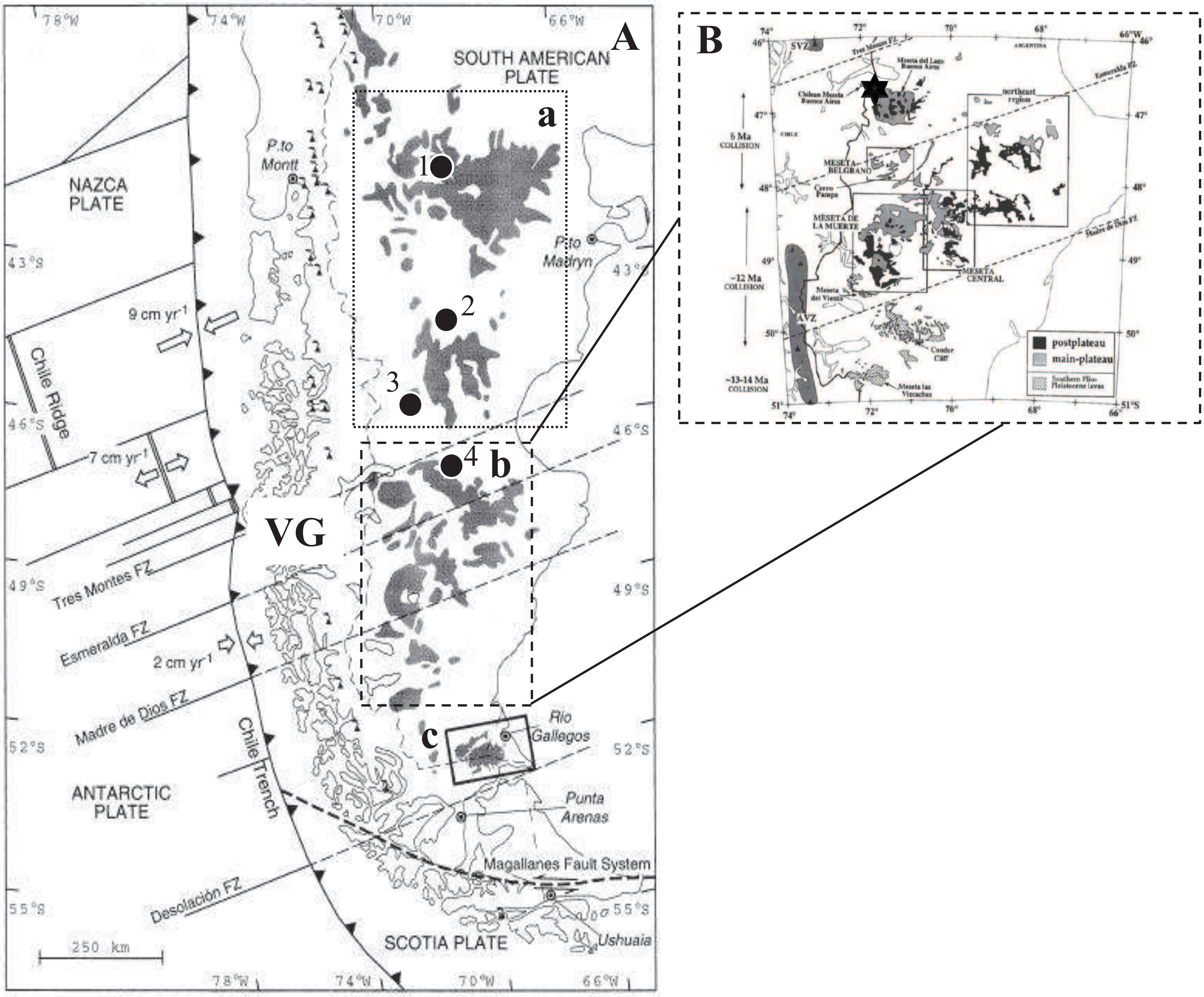

Fig. 1: Sketch map of Patagonia (**A,** after *D'Orazio et al., 2000*). VG stands for "Volcanic Gap". (**a**), (**b**) and (**c**) indicate the back-arc volcanic fields respectively of Northern Patagonia, Central Patagonia and Southern Patagonia. **1** Cerro Aznare; **2** Cerro Rio Chubut; **3** Cerro de los Chenques; **4** Cerro Clark. Sketch map **B** (from *Gorring et al., 1997*) shows the occurrence of the different plateau of Central Patagonia. In grey and black are represented the main and post-plateau sequences respectively. Black star localizes sampling site of xenoliths at Estancia Sol de Mayo (ESM).

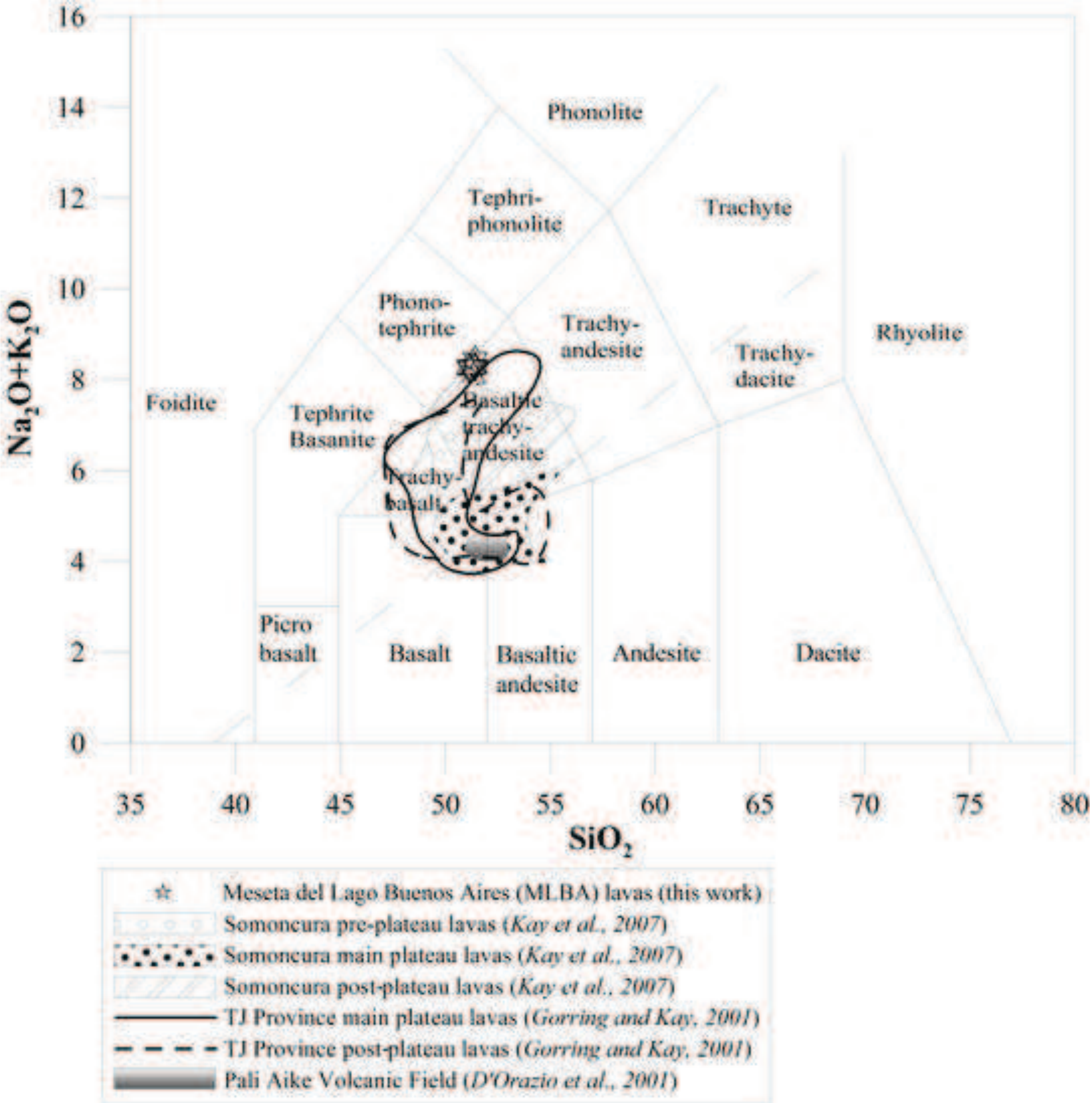

Fig. 2: Total alkali vs. silica diagram of Le Bas and Streckeisen (1991). Dash dot line separates the alkaline and subalkaline domains.

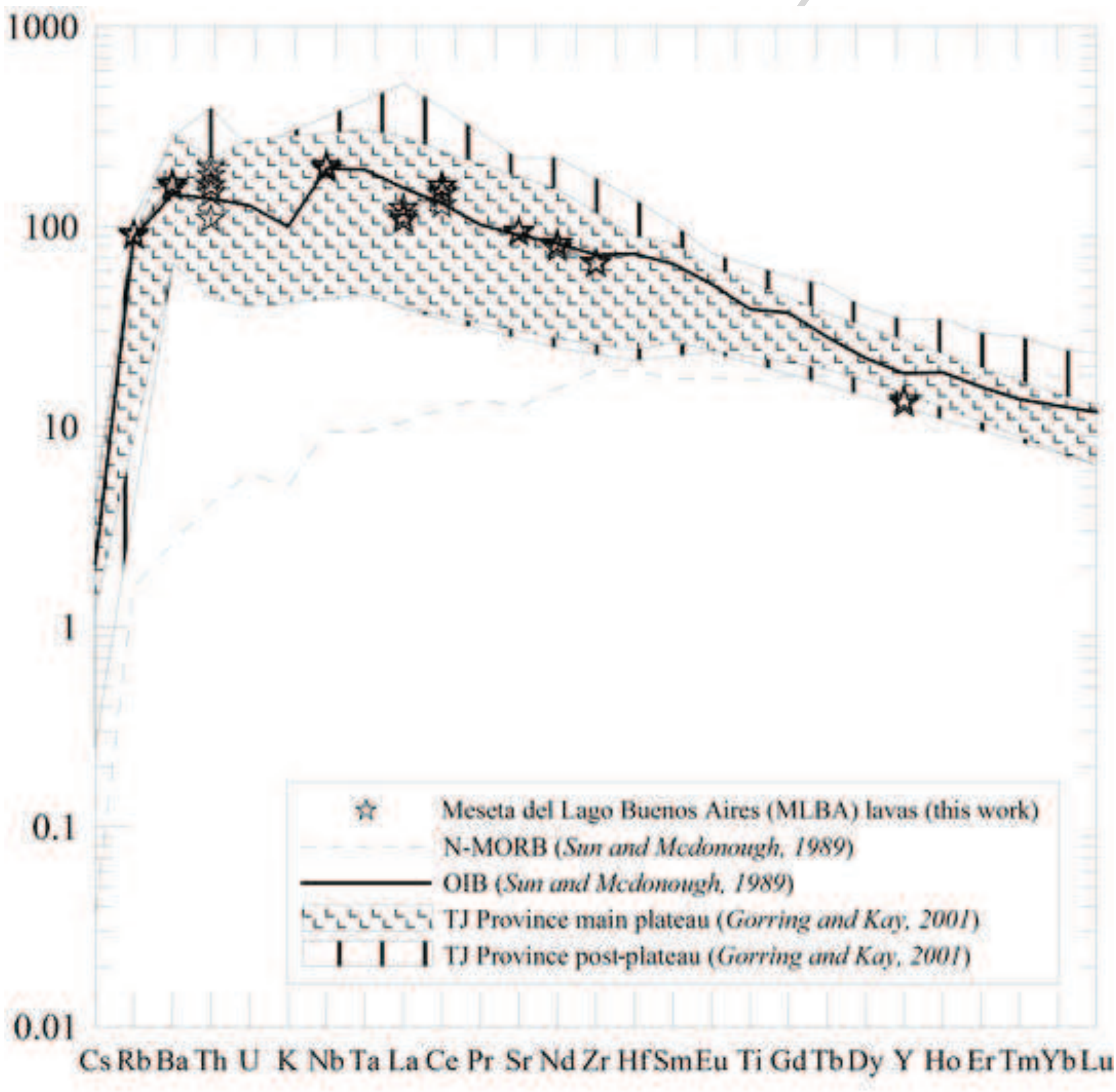

Fig. 3: Chondrite normalized (Sun and McDonough, 1989) trace element compositions of Meseta Lago Buenos Aires (MLBA) post-plateau lavas.

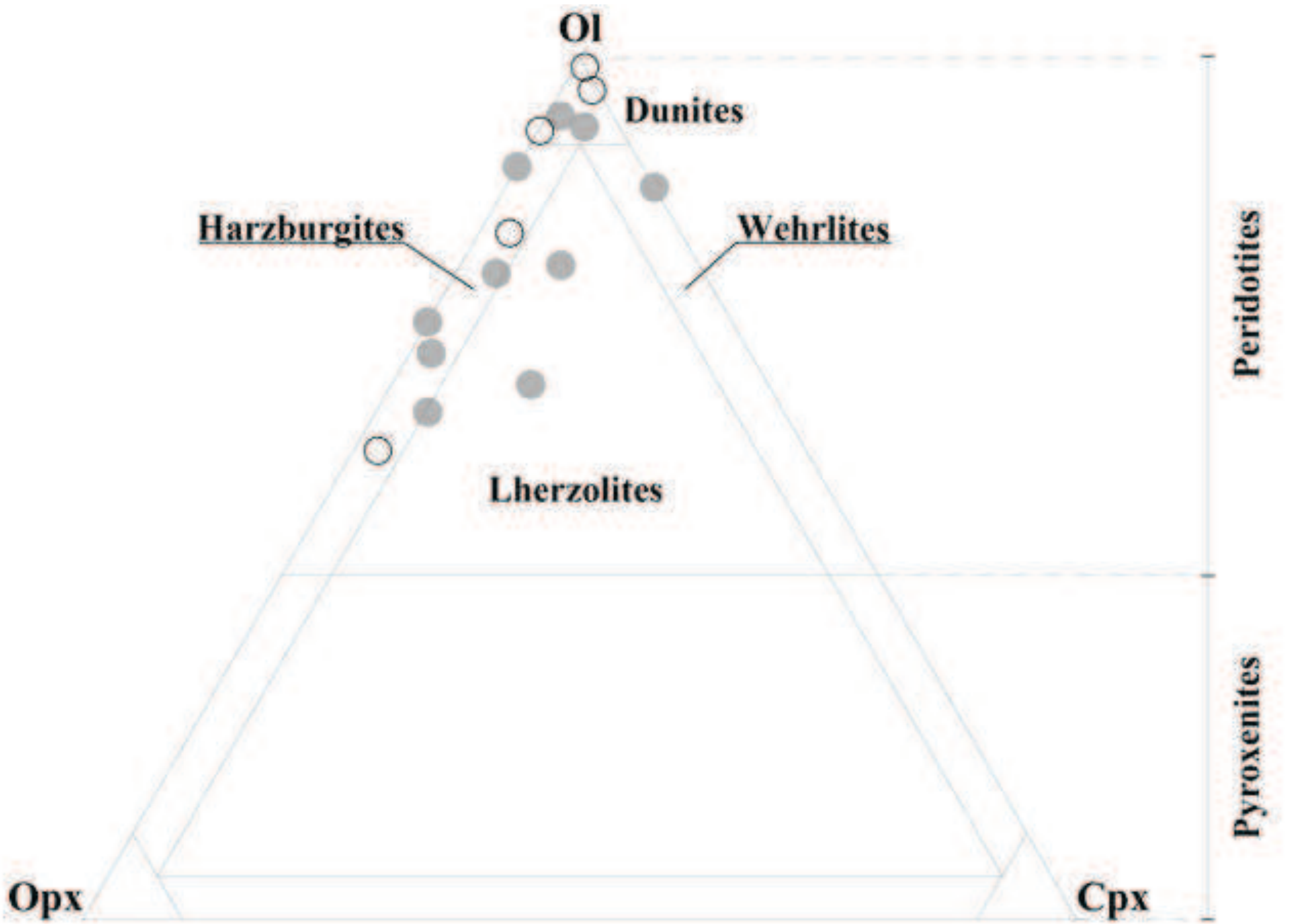

Fig. 4: Ultramafic classification diagram (after Streckeisen, 1976) of the Estancia Sol de Mayo (ESM) mantle xenoliths. Empty symbols indicate samples studied only petrographically, while full symbols indicate those studied both petrographically and geochemically.

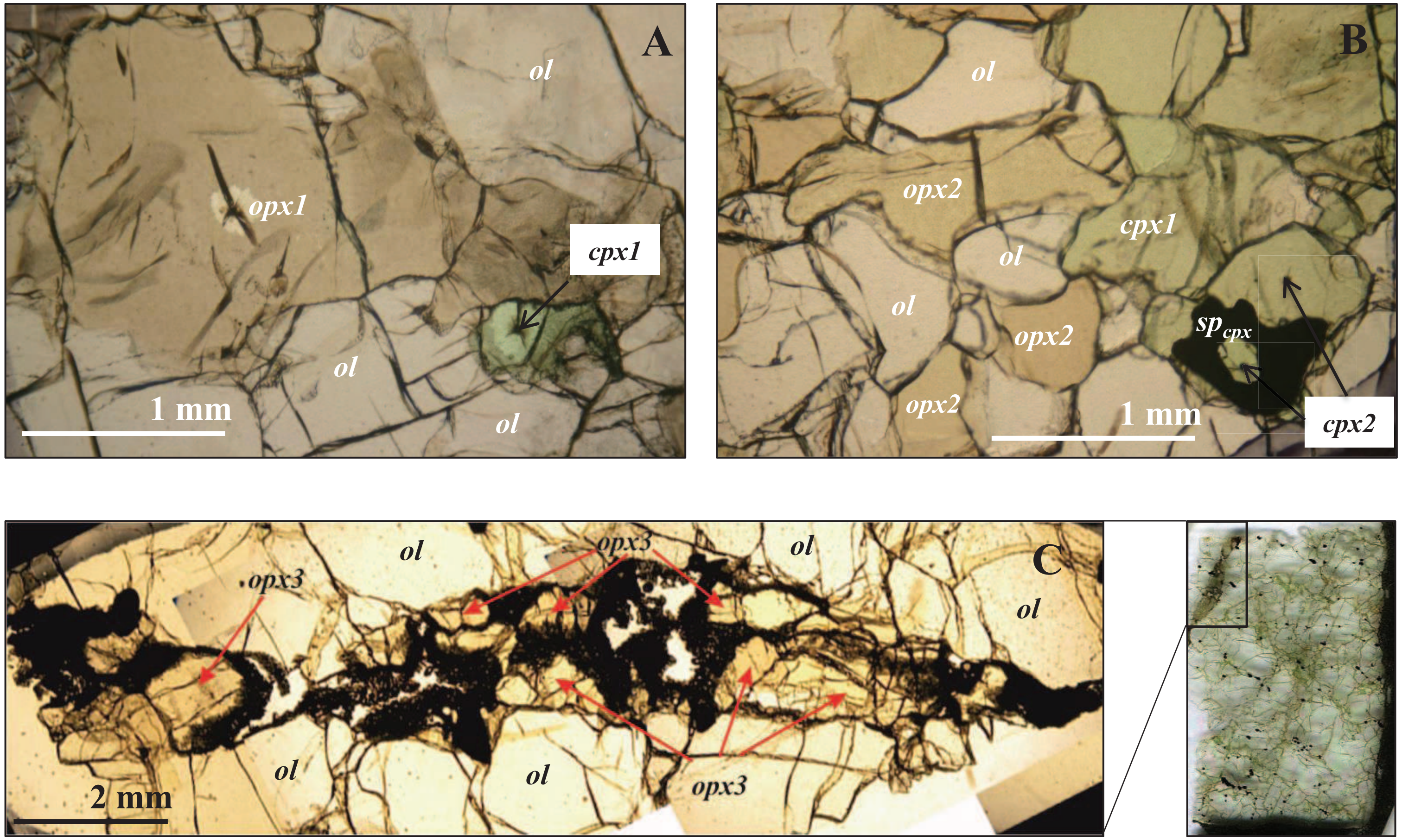

Fig. 5: Transmitted plane-polarized photomicrographs of representative assemblages in the Estancia Sol de Mayo (ESM) xenoliths. Ol, olivine; opx, orthopyroxene; cpx, clinopyroxene; sp, spinel. Cpx are further classified as cpx1 and cpx2. The former generally occur as protogranular in the peridotitic matrix, while the latter is observed around the sp. Opx is subdivided in opx1, opx2 and opx3: the first present as large protogranular crystals with exsolution lamellae while the second as small clean and undeformed grains without exsolution lamellae; the third occur as smaller grains arranged in vein. (**A**) Protogranular anhydrous spinel-bearing harzburgite MGP4b comprising ol, cpx1 and opx1. (**B**) Protogranular to porphyroclastic anhydrous spinel-bearing harzburgite MGP1b comprising ol, small porphyroclastic clean and undeformed grains of opx2, a cpx1 grain and a cpx2 growing around a black sp. (**C**) Vein of opx3 in dunite MGP2a. Opx3 are surrounded by a black matrix constituted by very small grains of ol, cpx and plagioclase.

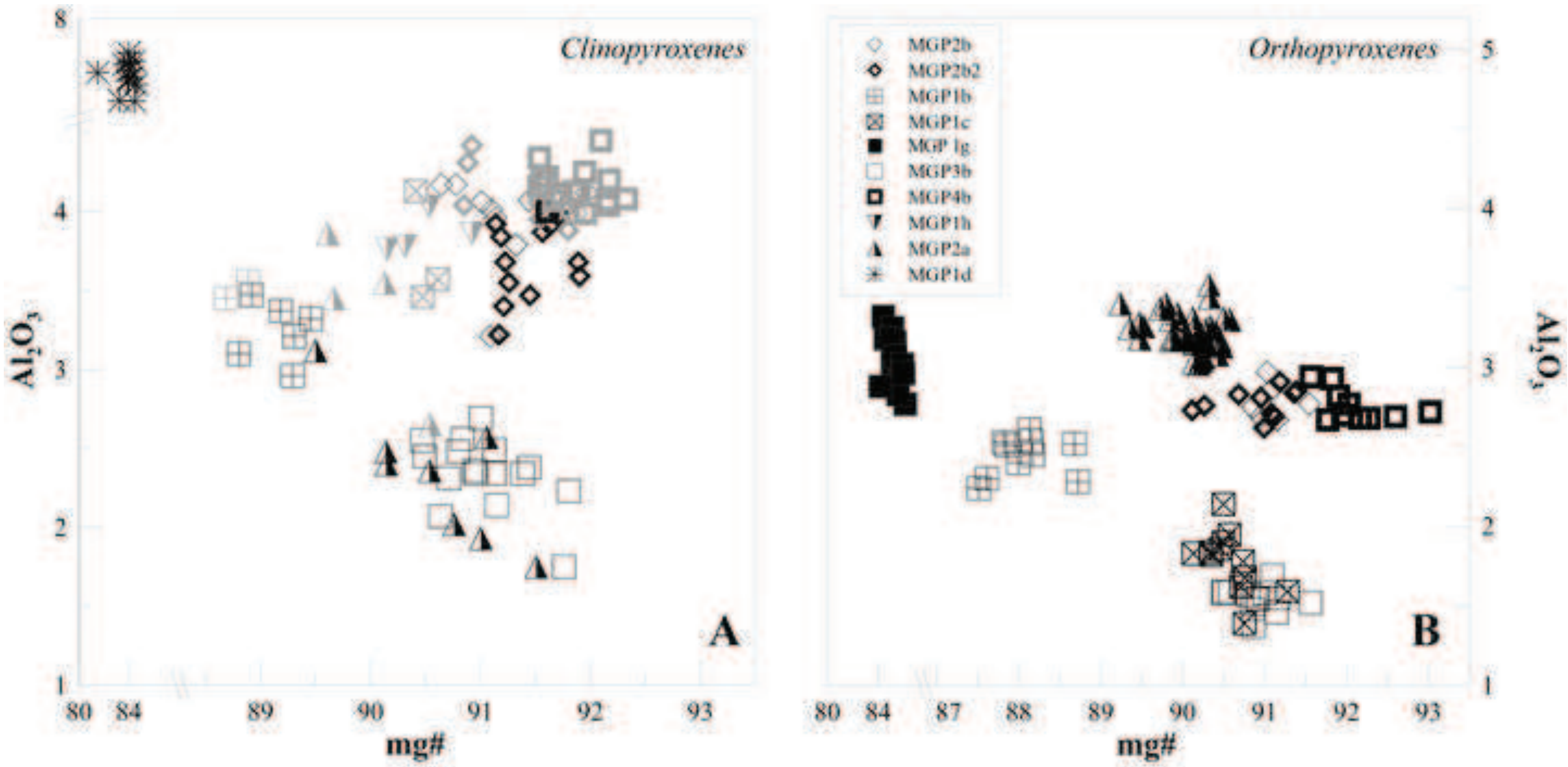

Fig. 6: Al_2O_3 vs mg# of clinopyroxenes and orthopyroxenes. Diamonds refer to lherzolites, squares to harzburgites, triangles to dunites and asterisk to wehrlite. In A, black symbols represent cpx1 while grey symbols cpx2.

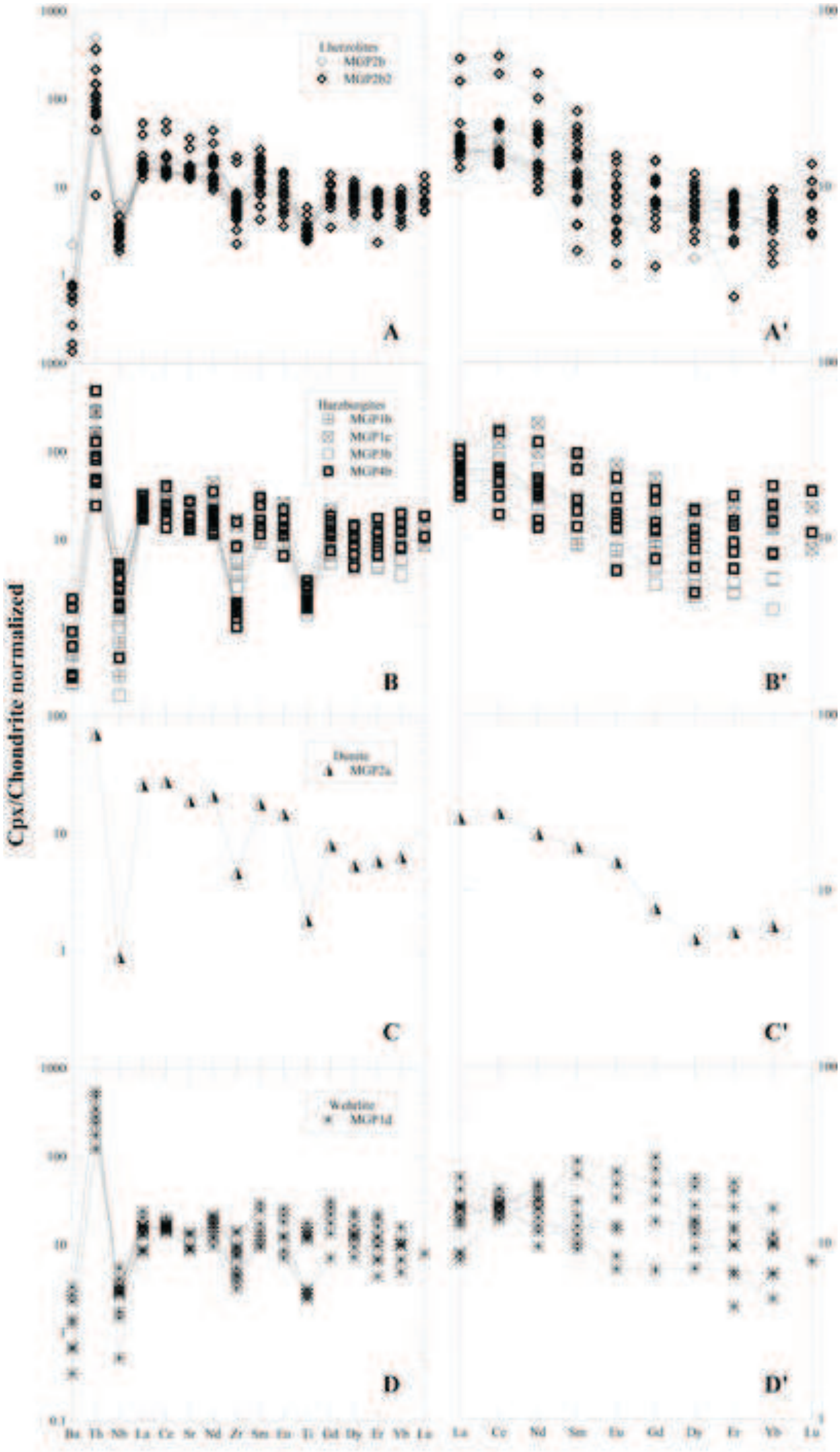

Fig. 7: Chondrite normalized (Sun and McDonough, 1989) incompatible trace elements (A, B, C, D) and REE (A', B', C', D') of clinopyroxenes

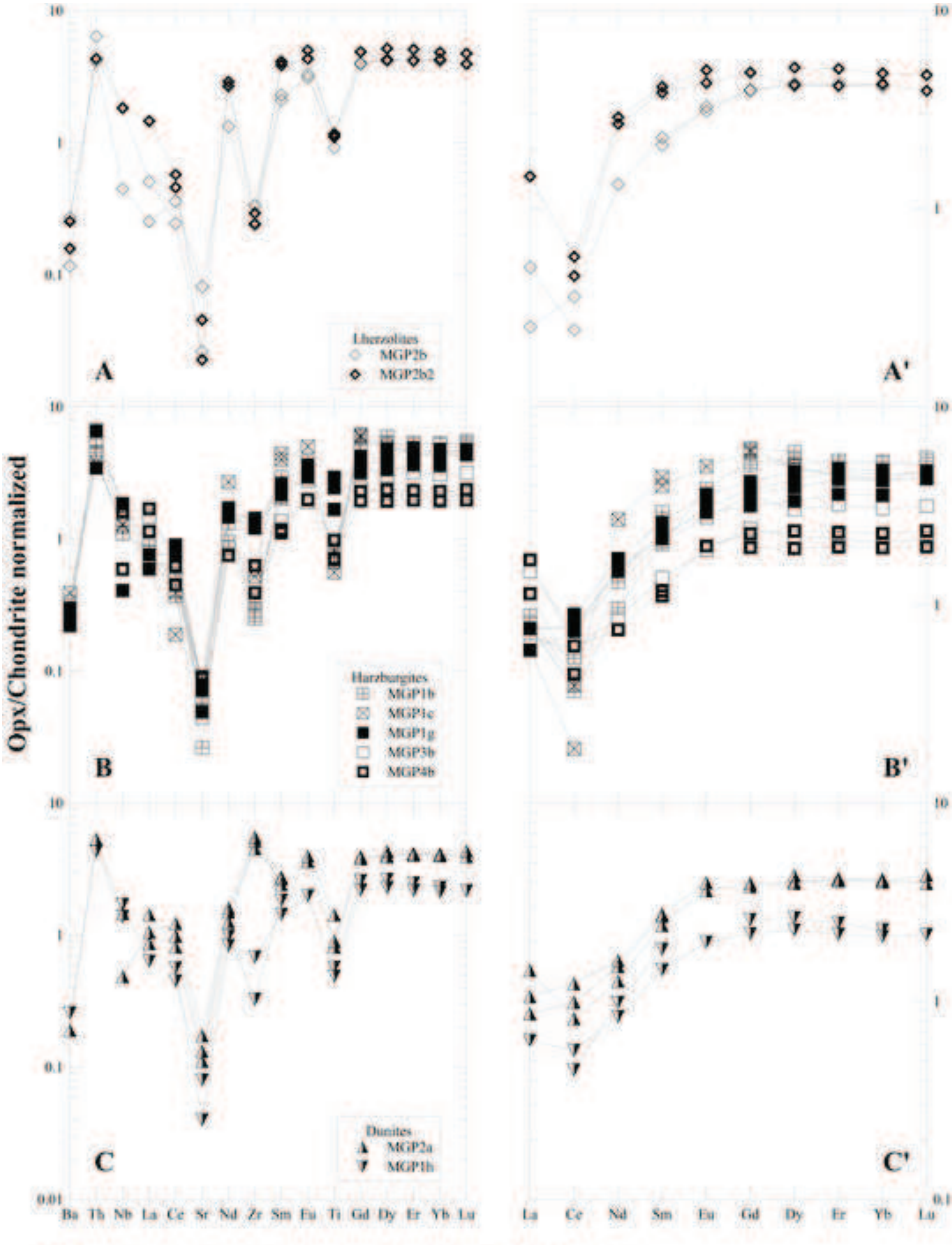

Fig. 8: Chondrite-normalized (Sun and McDonough, 1989) incompatible trace elements (A, B, C) and REE (A', B', C') of orthopyroxenes.

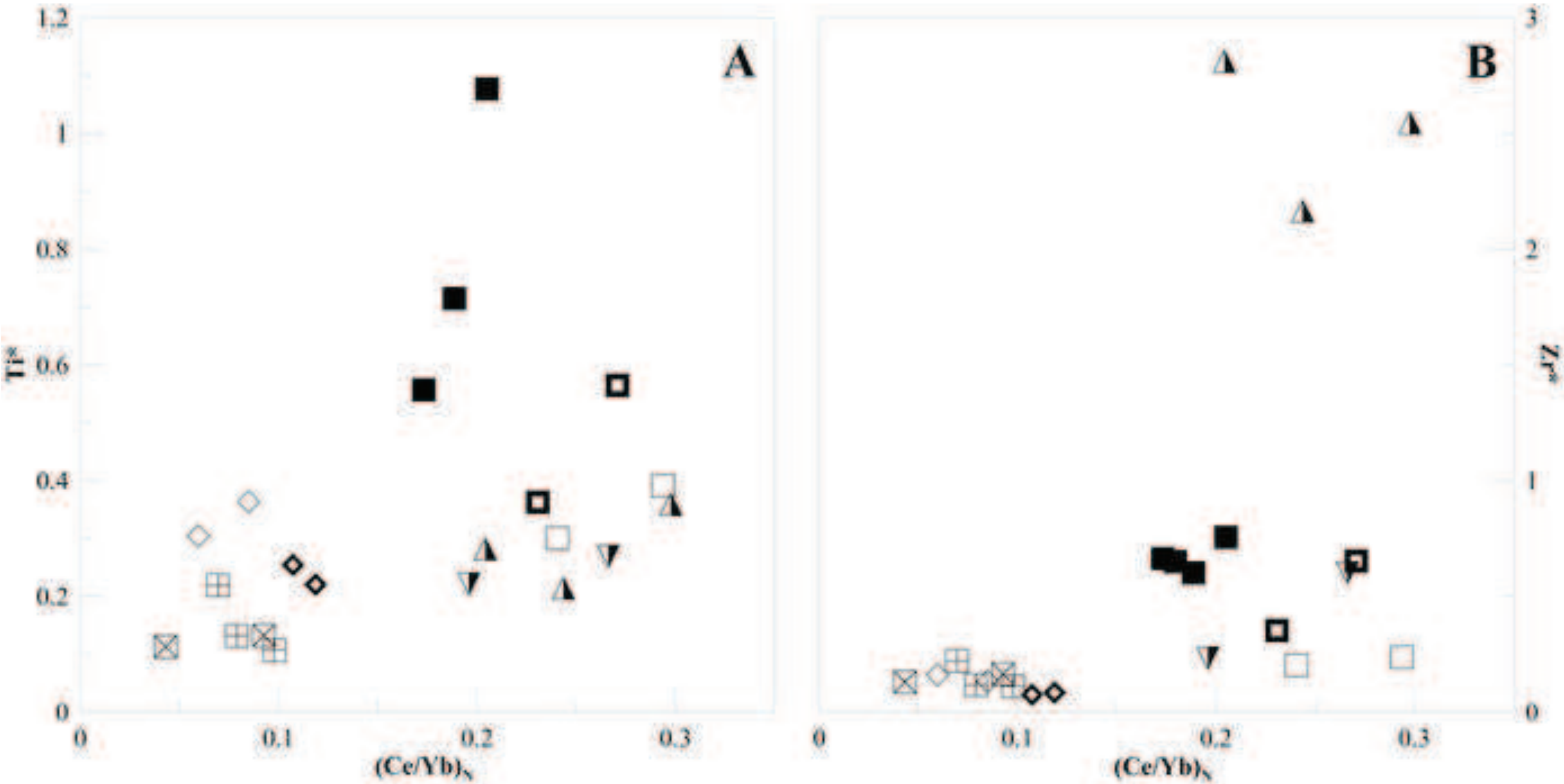

Fig. 9: Ti* (calculated as [Ti_N/((Eu_N+Gd_N)/2)]) and Zr* (calculated as [Zr_N/((Sm_N+Nd_N)/2)]) vs. (Ce/Yb)$_N$ for some selected orthopyroxenes from Estancia Sol de Mayo (ESM). For symbols refer to **Fig. 6**.

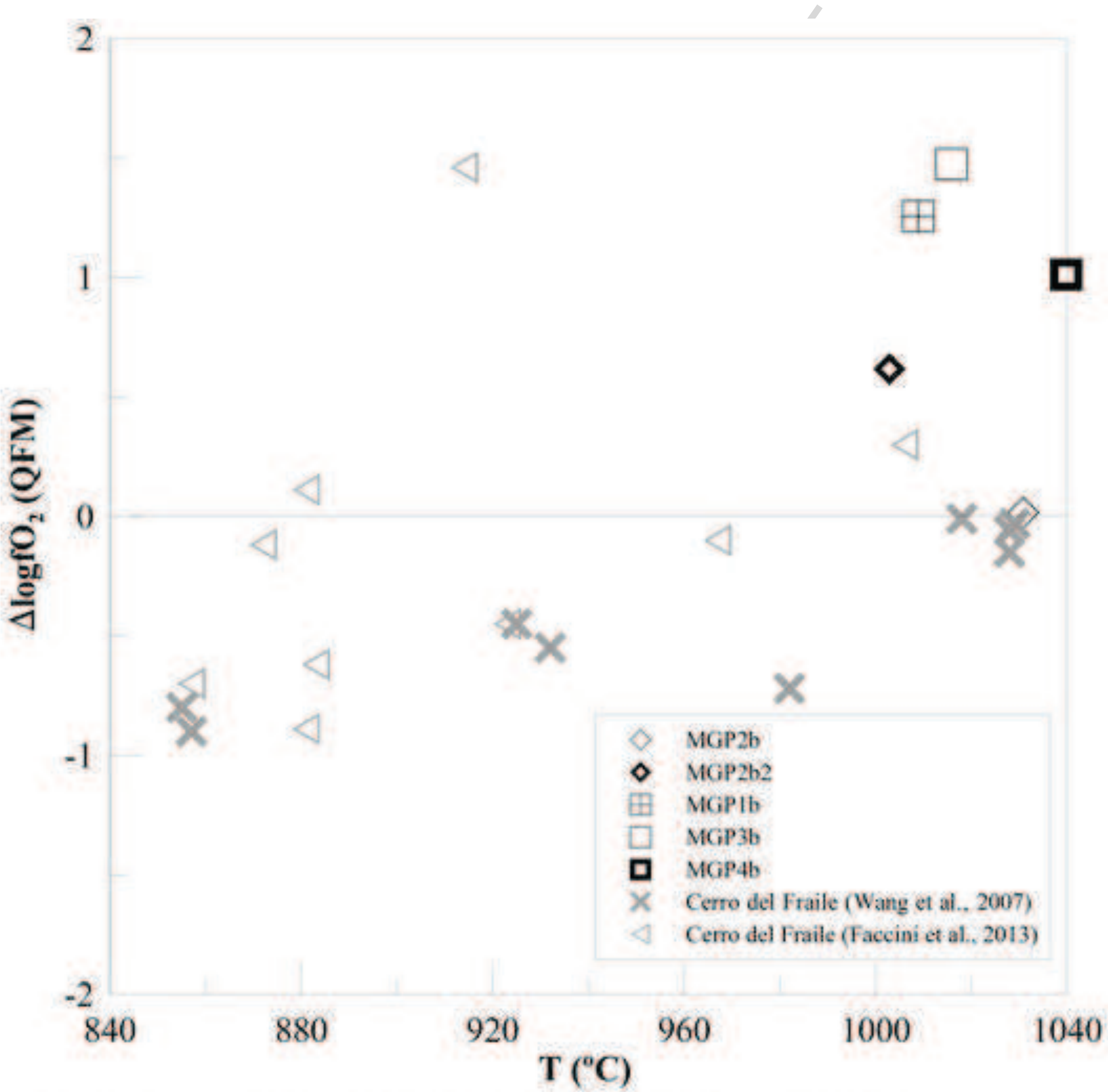

Fig. 10: Oxygen fugacity [calculated as $\Delta logfO_2$ (QFM) (Ballhaus et al., 1991)] vs. temperature (from Brey and Kölher, 1990) of Estancia Sol de Mayo (ESM) peridotites.
For comparison oxygen fugacity of Cerro del Fraile from Wang et al. (2007) and Faccini et al. (2013).

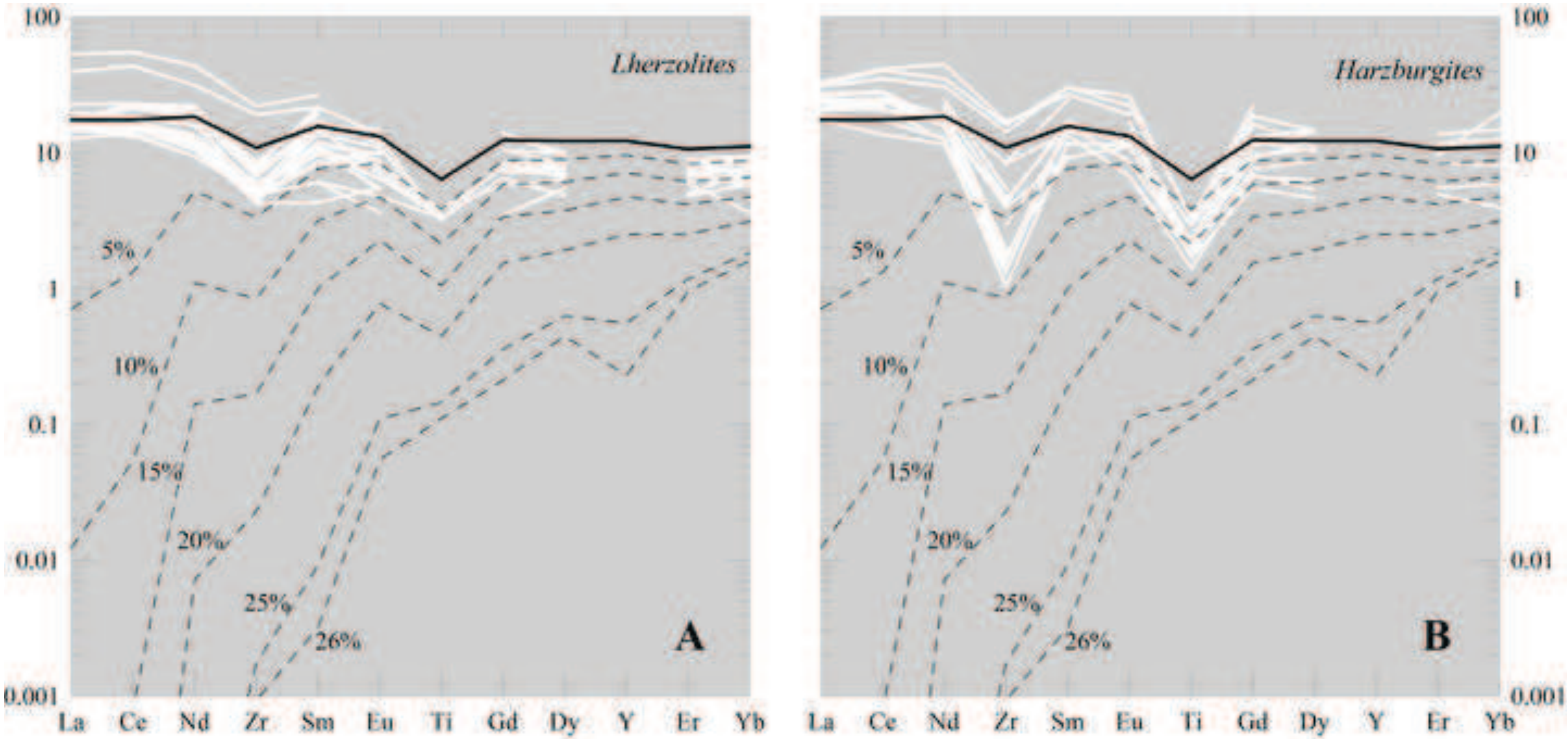

Fig. 11: Chondrite-normalized REE of cpx from Estancia Sol de Mayo (ESM, white lines) from lherzolites (A) and harzburgites (B) compared to the curves (black dashed lines) of 5%, 10%, 15%, 20%, 25% and 26% fractional partial melting (Johnson et al., 1990) of a starting fertile cpx (bold black line) from Bonadiman et al. (2005).

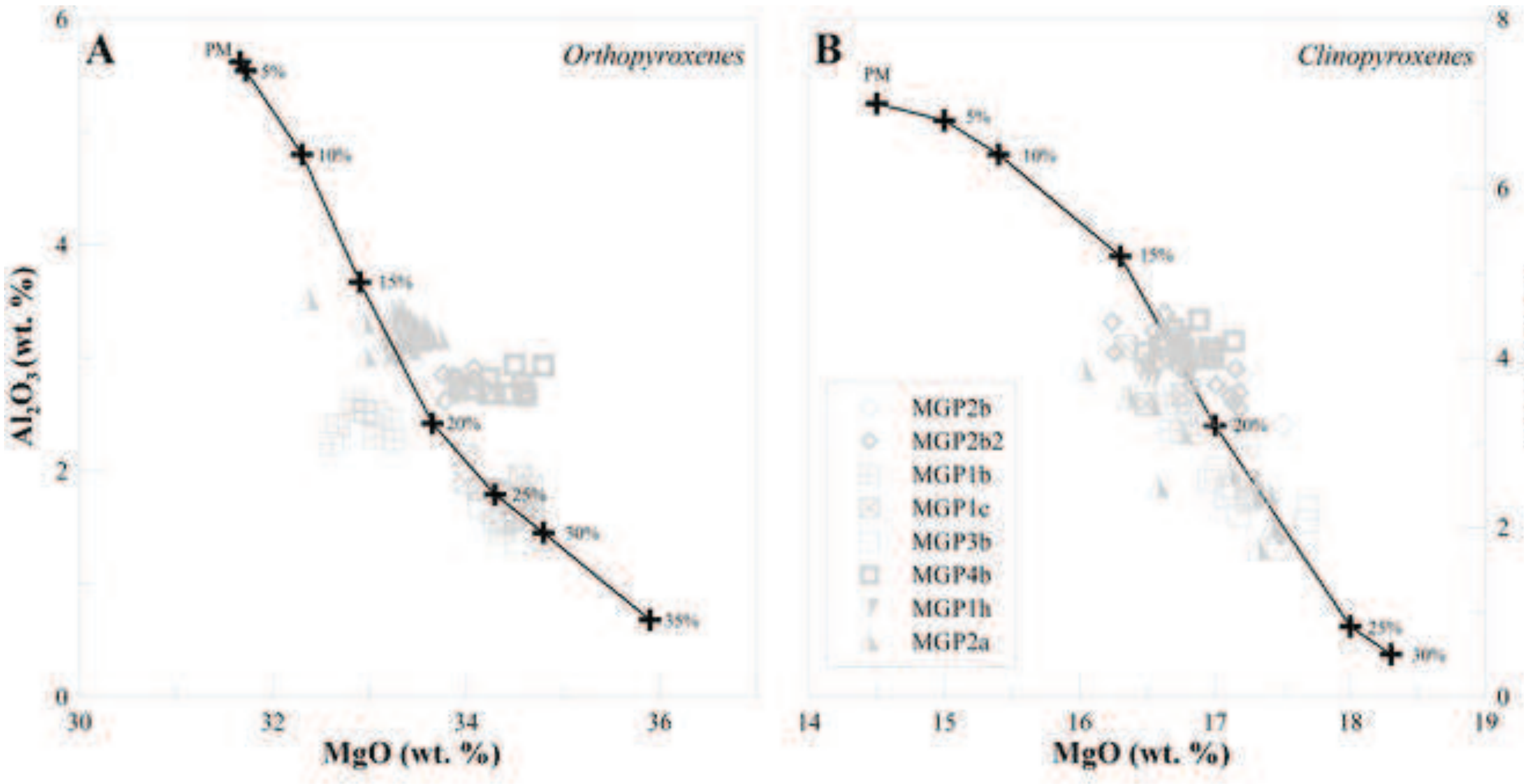

Fig. 12: Al_2O_3 vs MgO melting trends from Bonadiman et al., (2011) for opx and cpx in Estancia Sol de Mayo (ESM) mantle xenoliths. Primitive Mantle (PM) opx and cpx composition in terms of Al_2O_3 and MgO were calculated on the basis of the primitive mantle composition of McDonough & Sun (1995). Black crosses on curves indicate partial melting percentages.

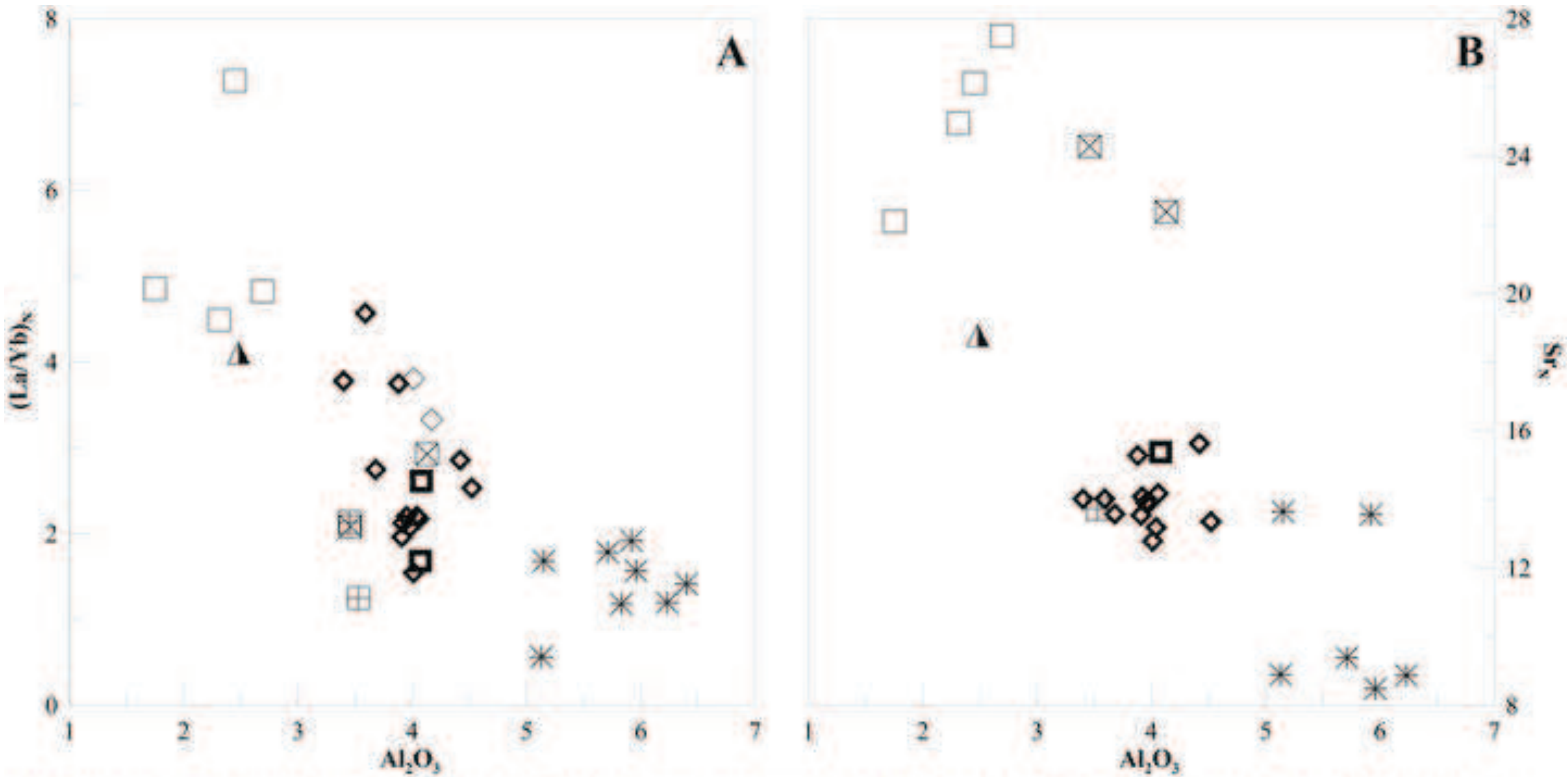

Fig. 13: Variation in some selected samples of $(La/Yb)_N$ and Sr_N vs. Al_2O_3 of clinopyroxenes. A negative correlation between the two geochemical markers and the content of Al_2O_3 is highlighted. For symbols refer to **Fig. 6**.

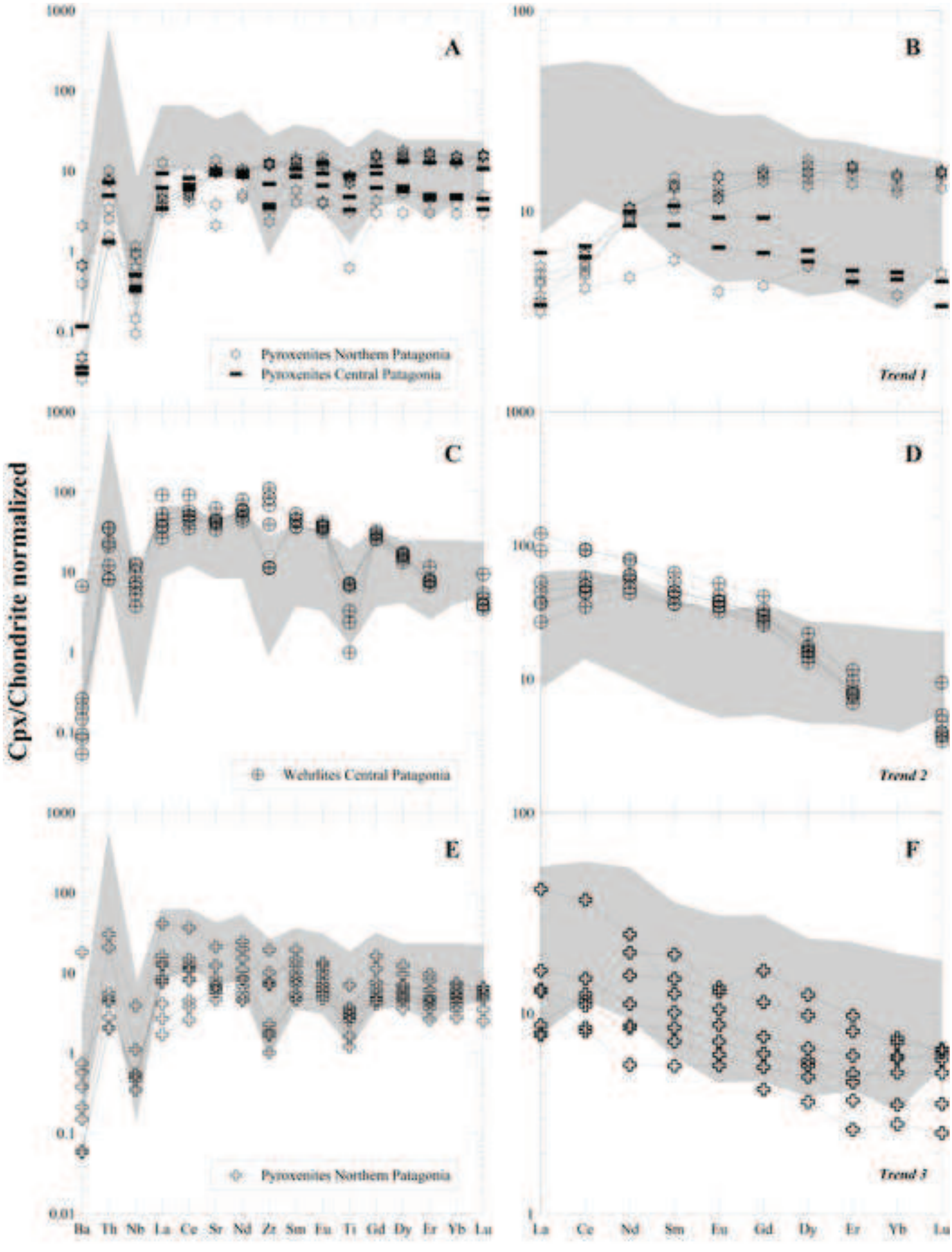

Fig. 14: Chondrite-normalized (Sun and McDonough, 1989) incompatible trace elements (A, C, E) and REE patterns (B, D, F) of clinopyroxenes from pyroxenites of Nothern and Central Patagonia and wehrlites from Central Patagonia (Dantas, 2007). Light grey field represents the clinopyroxenes from Estancia Sol de Mayo (ESM).

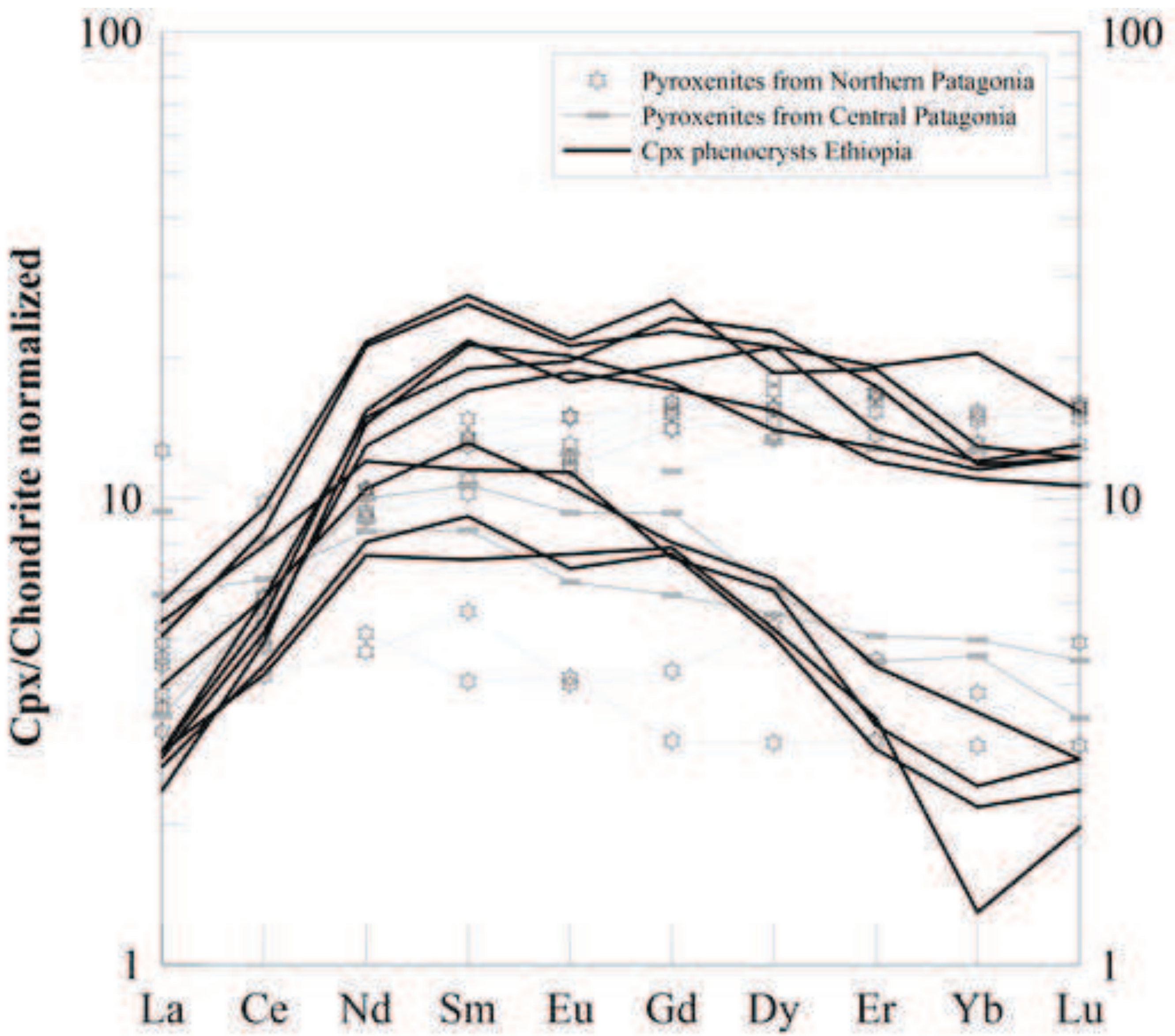

Fig. 15: Chondrite-normalized (Sun and McDonough, 1989) incompatible trace elements of clinopyroxenes from pyroxenites of Nothern and Central Patagonia (Dantas, 2007) and clinopyroxenes phenocrysts entrained in Northern Ethiopian continental flood basalts (from Beccaluva et al., 2004).

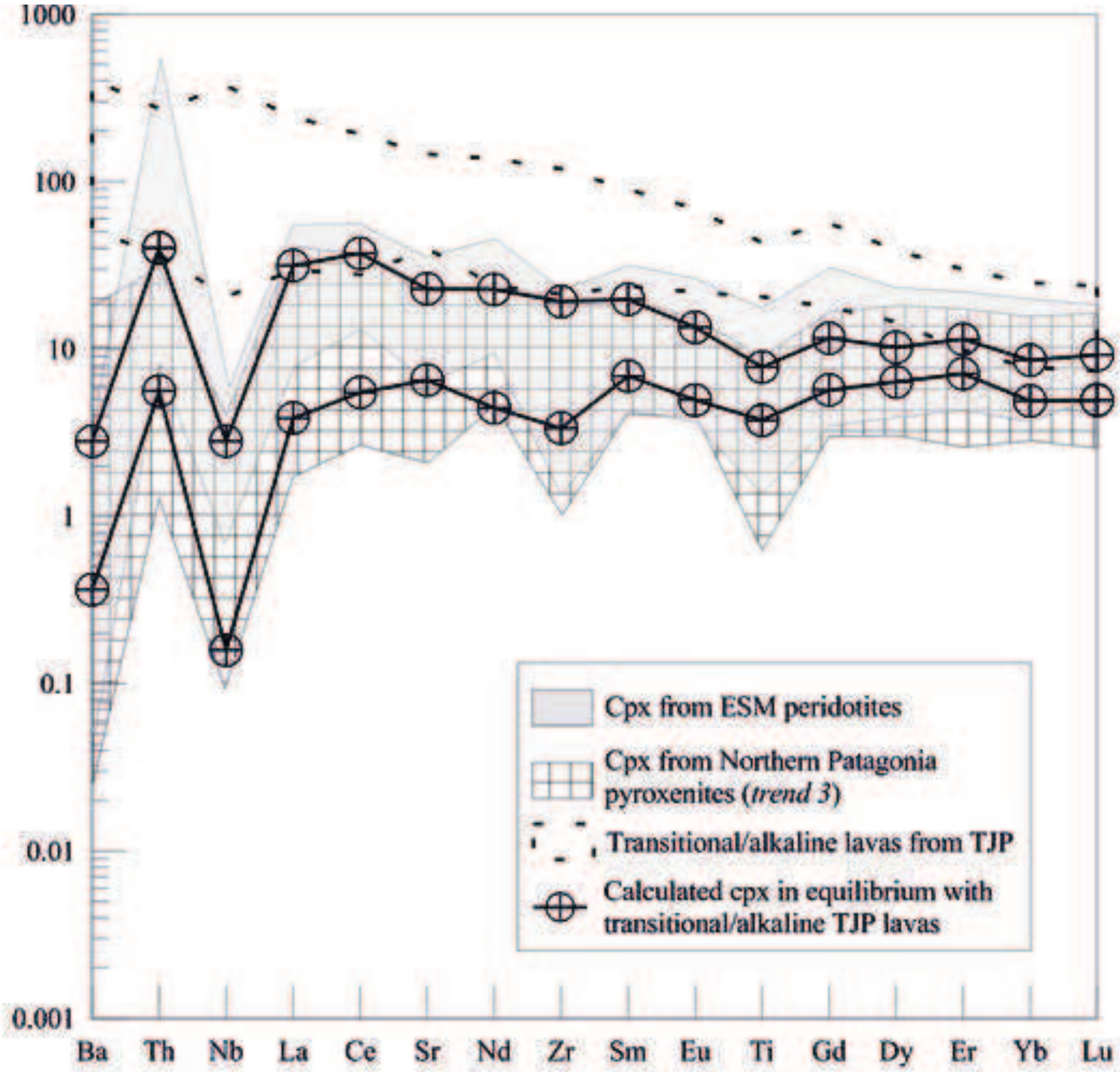

Fig. 16: Chondrite-normalized (Sun and McDonough, 1989) incompatible trace elements pattern reconstructions of clinopyroxenes from transitional/alkaline mafic lavas from the Triple Junction Province.

Highlights

- Two clinopyroxenes and three orthopyroxenes generations in Patagonian peridotites
- Al_2O_3 vs. mg# identify two different trends for clinopyroxenes and orthopyroxenes
- Clinopyroxenes in ESM peridotites match those of Northern Patagonia pyroxenites
- A refertilization process due to a transitional melt occurred at mantle depth